https://doi.org/10.5194/egusphere-2023-2060
Preprint. Discussion started: 16 November 2023

VISIR-2: ship weather routing in Python

Gianandrea Mannarini[1], Mario Leonardo Salinas[1], Lorenzo Carelli[1], Nicola Petacco[2], and Josip Orović[3]

[1]Ocean Predictions and Applications Division, CMCC, via Marco Biagi 5, 73100 Lecce, Italy
[2]DITEN, Università degli Studi di Genova, via Montallegro 1, 16145 Genova, Italy
[3]Maritime Department, University of Zadar, Ul. Mihovila Pavlinovića, 23000 Zadar, Croatia

Correspondence: Gianandrea Mannarini (gianandrea.mannarini@cmcc.it)

Abstract. Ship weather routing, which involves suggesting low-emission routes, holds potential for contributing to the decarbonisation of maritime transport. However, its quantitative impact has been explored only to a limited extent, also for a lack of readily deployable open-source and open-language computational models.

As a response, the VISIR model has been refactored in Python, incorporating new features. The velocity composition with currents has been refined, now encompassing leeway as well. For motor vessels, the angle of attack of waves has been considered, while sailboats now account for the combined effects of wind and sea currents. A least-CO_2 algorithm in presence of dynamic graph edge weights has been implemented and validated, proving a quasi-linear computational performance which outperforms VISIR-1. The software suite's modularity has been significantly improved, alongside a thorough validation against various benchmarks.

The resulting VISIR-2 model has been employed in numerical experiments within the Mediterranean Sea for the entire 2022, utilising meteo-oceanographic analysis fields. For a 125-meter-long ferry, the distribution of carbon dioxide savings follows a bi-exponential distribution. Two-digit CO_2 savings were possible for more than ten days in a year. Largest savings were achieved in avoiding upwind sailing and using the lowest engine load. In the case of an 11-meter sailboat, time savings increase with the extent of path elongation, particularly during upwind sailing. The sailboat's routes were approximately 3% shorter thanks to optimisation, and there was potential for additional savings when favourable currents were in play. The impact of leeway was minor, but disregarding it would result in a systematic underestimation of route durations.

VISIR-2 is a collaborative model with the capacity to harness knowledge from oceanography, ocean engineering, and computer science, to contribute to the decarbonisation efforts in the shipping industry.

1 Introduction

As climate change, with its unambiguous attribution to anthropogenic activities, rapidly unfolds (IPCC, 2023), the causal roles played by various sectors of the economy, as well as the possibilities for mitigation, are becoming more evident. This holds true for the shipping sector as well (IPCC, 2022), which has begun taking steps to reduce its carbon footprint. The International Maritime Organization (IMO) adopted an initial decarbonisation strategy in (IMO, 2018) which was later revised in 2023. The new ambition is to achieve complete decarbonisation by mid-century, addressing all greenhouse gas (GHG) emissions, with a partial uptake of near-zero GHG technology as early as 2030 (IMO, 2023). While no new measures have been adopted

https://doi.org/10.5194/egusphere-2023-2060
Preprint. Discussion started: 16 November 2023

yet, the revised strategy is expected to boost efforts to increase the energy efficiency of shipping in the short term (Smith and Shaw, 2023). In line with the European Green Deal, the European Union has adopted new rules to include various GHG (carbon dioxide, methane, and nitrous oxide) emissions from shipping in its Emissions Trading System (EU-ETS), starting from 2024*. For the first time ever, this will entail surrendering allowances for GHG emissions from vessels as well.

Besides financial incentives or penalties, achieving the decarbonisation of shipping will necessitate the widespread availability of zero- or low-carbon fuels. The estimated amount of clean energy required for the shipping sector is approximately 13 Exajoules, equivalent to one Terawatt of installed power from renewables†. This demand will not be easily met, and residual shipping emissions might have to be offset through carbon capture and storage (Zhou and Wang, 2014). Moreover, zero-emission bunker fuels are projected to cost significantly more than present-day fossil fuels (Al-Aboosi et al., 2021; Svanberg et al., 2018). Thus, minimising their use will be crucial for financial sustainability. This necessitates energy savings through efficient use, achieved via both technical (e.g., wind-assisted propulsion or WASP) and operational measures (e.g., speed reduction and ship weather routing). According to the CE-Ship model, a global reduction of GHG emissions by 2030 by up to 47% relative to 2008 levels could be feasible through a combination of operational measures, technical innovations, and the use of near-zero-GHG fuels (Faber et al., 2023). A separate study focusing on the European fleet estimates that a reduction of sailing speed alone could potentially lead to a 4-27% emission reduction, while combining technical and operational measures might provide an additional 3-28% reduction (Bullock et al., 2020). The impact of speed optimisation on emissions varies significantly, with potential savings ranging from one third to as high as 80%, depending on factors such as the actual route, meteorological and marine conditions, and the vessel type (Bouman et al., 2017). On the other hand, while cases are reported of up to 50% savings, the role of weather routing is generally assessed to be lower than 10%. The variability in savings can be attributed to the diversity of routes considered, the specific weather conditions, and the type of vessels analysed. Additionally, reviews often use a wide range of bibliographic sources, including grey literature, company technical reports, white papers, and works that fail to address the actual meteorological and marine conditions.

The VISIR (discoVerIng Safe and effIcient Routes) ship weather routing model was designed to objectively assess the potential impact of oceanographic and meteorological information on the safety and efficiency of navigation. So far, two versions of the model have been released (VISIR-1.a, Mannarini et al. (2016a), and VISIR-1.b, Mannarini and Carelli (2019)). However, the use of a proprietary coding language (Matlab) may hinder its further adoption. Also, the experience with VISIR-1 suggested the need to enhance the modularity of the package and implement other best practices of scientific coding, as recommended in Wilson et al. (2014). Another area where innovation seemed possible was the development of a comprehensive framework to perform weather routing for both motor and sailboats using the same computational platform. While some aspects of this were covered through a more modular approach, it also required a rethinking of how to utilise environmental fields such as waves, currents, and wind. Furthermore, while the carbon savings of least-time routes were already estimated via VISIR-1.b, a dedicated algorithm for the direct computation of least-CO_2 was lacking.

*https://climate.ec.europa.eu/eu-action/transport-emissions/reducing-emissions-shipping-sector_en (Interinstitutional negotiations)
†https://cms.zerocarbonshipping.com/media/uploads/publications/Maritime-Decarbonization-Strategy-2022.pdf

https://doi.org/10.5194/egusphere-2023-2060
Preprint. Discussion started: 16 November 2023

To address all these requirements, we designed, coded, tested, and conducted extensive numerical experiments with the VISIR-2 model. VISIR-2 is a Python-coded software, inheriting from VISIR-1 the fact that it is based on a graph-search method. However, VISIR-2 is a completely new model, leveraging the previous experience, while also offering many new solutions and capabilities. Part of the validation process made use of its ancestor model. The computational performance has been enhanced, and efforts have been made to improve usability. VISIR-2 features are thoroughly described in this paper, along with some case studies and hints for possible development lines in the future.

The remainder of this paper comprises a literature investigation in Sect. 1.1, followed by an in-depth presentation of the innovations introduced by VISIR-2 in Sect. 2. Subsequently, the model validation is discussed in Sect. 3 and its performance assessment is provided in Sect. 4. Several case studies in the Mediterranean Sea follow (Sect. 5). Finally, the conclusions and outlook are presented in Sect. 6. An Appendix contains technical information regarding the computation of the angle of attack between ship's heading and course (App. A), as well as details about the neural network employed to identify the vessel performance curves (App. B).

1.1 Literature review on weather routing

This compact review of systems for ship weather routing will be limited to web applications (Sect. 1.1.1) and peer-reviewed research papers (Sect. 1.1.2). It is further restricted to the free available versions of desktop applications, while the selection of papers is meant to update the wider reviews already provided in Mannarini et al. (2016a); Mannarini and Carelli (2019). A critical gap analysis (Sect. 1.1.3) completes this subsection.

1.1.1 Web applications

FastSeas[‡] is a weather routing tool for sailboat, with editable polars, and possibility to consider a motor propulsion. Wind forecasts are taken from the NOAA GFS model and ocean surface currents from OSCAR. It makes use of Windy.com imagery, a free choice of endpoints is offered, departure time can vary between present and a few days in the future, the voyage-plan is exportable in various formats.

The AVALON web router[§] provides a coastal weather routing service for sailboats, within subregions of France, United Kingdom, and United States. It offers a choice among tens of sailboats, with the option to consider also a motor-assisted propulsion. Hourly departure dates within a couple of days are allowed, and ocean weather along the routes is provided in tabular form.

GUTTA-VISIR[¶] is a weather routing tool for a specific ferry. It provides both least-time and least-CO_2 routes between several ports of call. It makes use of operational wave and current forecast fields from the Copernicus Marine Environment Monitoring Service (CMEMS). The route departure date and time and the engine load can be varied. Waves, currents, or isolines can be rendered along with the routes, which can be exported.

[‡]https://fastseas.com/
[§]https://www.webrouter.avalon-routing.com/compute-route
[¶]https://gutta-visir.eu

https://doi.org/10.5194/egusphere-2023-2060
Preprint. Discussion started: 16 November 2023

openCPN[‖] is a comprehensive open-source platform, including also a weather routing tool for sailboats. The boat is represented via polars, and forecast data in grib format or a climatology can be used. Nautical charts can be downloaded and integrated into the graphical user interface. The programming language is C++ and a velocity composition with currents is accounted for. A detailed documentation of the numerical methods used is lacking, though.

1.1.2 Research papers

A review of ship weather routing methods and applications was provided by Zis et al. (2020). Several routing methods such as the isochrone method, dynamic programming, calculus of variations, and pathfinding algorithms were summarised, before a taxonomy of related literature was proposed. The authors made the point that the wide range of emission savings reported in literature might in future be constrained via defining a baseline case, providing benchmark instances, and performing sensitivity analyses, e.g. on the resolution of the environmental data used.

A specific weather routing model was documented by Vettor and Guedes Soares (2016). It integrates advanced seakeeping and propulsion modelling with multi-objective (fuel consumption, duration, and safety) optimisation. An evolutionary algorithm was used, with initialisation from both random solutions and single-objective routes from a modified Dijkstra's algorithm. Safety constraints were considered via probabilities of exceeding thresholds for slamming, green water, or vertical acceleration. A specific strategy was proposed to rank solutions within a Pareto frontier.

A stochastic routing problem was addressed in Tagliaferri et al. (2014). A single upwind leg of a yacht race is considered, with the wind direction being the stochastic variable. The vessel was represented in terms of polars and the optimal route was computed via dynamic programming. The skipper's risk attitude was modeled via a specific preference on the wind transition matrices. This way it was shown how the risk attitude affects the chance to win a race.

Ladany and Levi (2017) developed a dynamic programming approach to sailboat routing which accounts for the tacking time. The latter was assumed to be proportional to the amplitude of the course change. Furthermore, a sensitivity analysis was conducted, considering both the uncertainty on wind direction and the magnitude of the discretisation step in the numerical solution.

Sidoti et al. (2023) provided a consistent framework for a dynamic programming approach for sailboats, considering both leeway and currents. In order to constrain the course of the boat on the available edges on the numerical grid, an iterative scheme was adopted. Case studies with NAVGEM winds and Global HYCOM currents were carried out in a region across the Gulf Stream. The results without leeway were validated versus openCPN.

The impact of stochastic uncertainty on WASP ships was addressed by Mason et al. (2023). A dynamic programming technique was used, and "a priori" routing (whereby information available at the start of the journey only is used) was distinguished from "adaptive" routing (whereby the optimum solution is updated based on information that becomes available every 24 h along a journey). The latter strategy is shown, for voyages lasting several days, to be more robust with respect to the unavoidable stochastic uncertainty of the forecasts.

[‖] https://opencpn.org/

https://doi.org/10.5194/egusphere-2023-2060
Preprint. Discussion started: 16 November 2023

1.1.3 Knowledge gap

A few open web applications exist, mainly for sailboats, and with limited insight into the numerical methods. Case studies results from weather routing systems developed in the academia were published, but (exception of Mason et al. (2023)) no systematic assessment of CO_2 savings was provided. Furthermore, no related software was disclosed in any case. A prevalence of dynamic programming approaches is noted, especially for web applications, with graph-search method being used in research papers only. The tools either focus on sailboats (with or without a motor) or on motor vessels. When both are available (such as in Fastseas), the motorboat is described in terms of polars.

From this assessment, an open-source and well-documented ship weather routing model, for both motor- and sailboats, with flexible characterisation of vessel performance, appears as a gap which the present work aims to close.

2 Technical advancements

This section includes a revision of the vessel kinematics of VISIR, as given in Sect. 2.1; changes in the graph generation procedure and in the use of static environmental fields in Sect. 2.2; updates to the computation of graph edge weights in Sect. 2.3; an additional optimisation objective in the shortest path algorithm in Sect. 2.4; new vessel performance models in Sect. 2.5; innovative visualisation capabilities in Sect. 2.6; and a more modular structure of the software package, presented in Sect. 2.7. Further technical details of the VISIR-2 code are presented in the software manual, provided along with its online repository.

2.1 Kinematics

For VISIR to deal with waves, currents, and wind, for both motor- and sailboats, several updates to its approach for velocity composition were needed. They included both generalisations and use of new quantities, addressed in this subsection, as well as a new numerical solution, addressed in App. A.

As in Mannarini and Carelli (2019), the kinematics of VISIR-2 is based on both the principle of superposition of velocities and the discretized sailing directions existing on a graph. However, while previously the vessel's speed over ground (SOG) was obtained from the vector sum of speed through water (STW) and ocean current ($\boldsymbol{w}$), we here show that, more generally, SOG results from the vector sum of the forward speed $\boldsymbol{F}$ and an effective current $\boldsymbol{\omega}$, and both will be defined in the following. In the absence of leeway, the $\boldsymbol{F}$ and STW vectors are identical and $\boldsymbol{\omega} = \boldsymbol{w}$, so the latter approach encompasses the former.

Making reference to Fig. 1, the use of a graph constrains the vessel's course over ground to be along $\hat{e}$, being the orientation of one of the graph's arcs. Thus, any cross-component of velocity, or along a $\hat{o}$ versor such that $\hat{e} \cdot \hat{o} = 0$, must be null. This implies that, to balance the cross flow from the currents, the vessel must head into a direction $\hat{h}$ slightly different from the course $\hat{e}$. In Mannarini and Carelli (2019) such an angle of attack was defined as

$$\delta = \psi_s - \psi_e \tag{1}$$

https://doi.org/10.5194/egusphere-2023-2060
Preprint. Discussion started: 16 November 2023

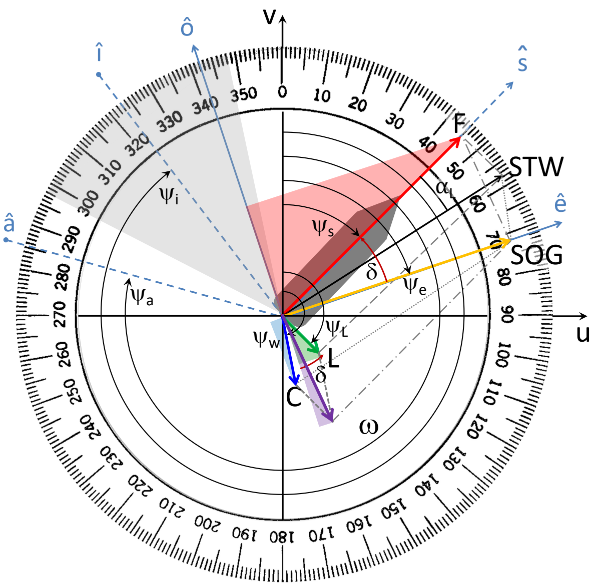

Figure 1. Angular configuration with ($\delta = -27°$, $\gamma_i = -109°$), resulting in $\epsilon = +1$. The dark grey area represents the ship hull, while the light grey shaded area denotes the no-go zone for $\alpha_0 = 25°$. Clockwise-oriented arcs indicate positive angles, and filled circles at line ends denote the meteorological ("from") convention.

where for both ψ_s (heading, or HDG), ψ_e (course over ground, or COG) a nautical convention is used (due North, to-direction). That framework is here generalised to also deal with the vector nature of some environmental fields, such as waves or wind. Using a meteorological convention (due North, from-direction) for both the ψ_a (waves) and ψ_i (wind) directions, we here introduce the δ_f angles, defined as

$$\delta_f = \psi_s - \psi_f = \delta - \gamma_f \tag{2}$$

where $\gamma_f = \psi_f - \psi_e$ are the relative angles between the f environmental field and the ship's course, with $f = a$ for waves and $f = i$ for wind. In computing angular differences, their convention should be considered (see `angular_utils.py` function in the VISIR-2 code). Thus, $\delta_f = 0$ whenever the ship heads into the direction from which the field comes, and $\gamma_f = 0$ if her course is into such a direction.

Furthermore, we here define leeway as a motion, caused by the wind, transversal to the ship's heading. From the geometry shown in Fig. 1, the oriented direction of leeway ψ_L is given by

$$\psi_L = \psi_s + \frac{\pi}{2} \cdot \epsilon \tag{3}$$

with

$$\epsilon = \cos\left(\pi \lfloor \delta_i / \pi \rfloor\right) \tag{4}$$

https://doi.org/10.5194/egusphere-2023-2060
Preprint. Discussion started: 16 November 2023

where the $\lfloor\cdot\rfloor$ delimiters indicate the floor function. Thus, ϵ is positive for δ_i in the $[0,\pi]$ range and flips every 180° of the argument. This is not the sole possible definition of leeway. For instance, in Breivik and Allen (2008) a distinction between downwind and crosswind component of leeway is made. However, the present definition is consistent with the subsequent data of vessel performance (Sect. 5.2.2).

Upon expressing the modules of the vessel's forward speed F and of leeway velocity L as

$$F = F(|\delta_i|, V_i; |\delta_a|, H_s, \chi) \tag{5a}$$

$$L = L(|\delta_i|, V_i), \tag{5b}$$

a leeway angle, being the ship's heading change between the $\boldsymbol{F}$ and STW vectors, can be defined as

$$\alpha_L = \mathrm{atan}(L/F) \tag{6}$$

The above introduced α_L is not a constant but depends on both wind magnitude V_i and the module of the relative direction, $|\delta_i|$. Also, from Fig. 1, it is seen that F = STW$\cdot\cos\alpha_L$. Thus, in the absence of leeway, one retrieves the identity of F and STW which was an implicit assumption done in Mannarini and Carelli (2019).

Eq. 5 is a major innovation with respect to the formalism of Mannarini and Carelli (2019), as an angular dependence in the vessel performance is introduced in VISIR also for motorboats for the first time (Sect. 2.5). Eq. 5a include dependencies on both wind and waves. Furthermore, a possible dependency on χ, the fractional engine load (or any other propulsion parameter), is here highlighted.

Within this formalism, if the vessel is a sailboat (or rather a motor vessel making use of WASP), just an additional condition should be considered. That is, given the wind-magnitude dependent no-go angle $\alpha_0(V_i)$, upwind navigation is not permitted, or:

$$\psi_s \notin [\psi_i - \alpha_0, \psi_i + \alpha_0] \tag{7}$$

Now, given a water flow expressed by the vector:

$$\boldsymbol{w} = C\,\hat{w} = (u, v)^T, \tag{8}$$

and making reference to Fig. 1, the flow projections along ($\hat{e}$) and across ($\hat{o}$) the vehicle course respectively are

$$w_{\parallel} = C\cos(\psi_e - \psi_w) = u\sin(\psi_e) + v\cos(\psi_e), \tag{9a}$$

$$w_{\perp} = C\sin(\psi_e - \psi_w) = v\sin(\psi_e) - u\cos(\psi_e), \tag{9b}$$

where also for the ocean flow direction ψ_w the nautical convention is used.

In analogy to Eq. 9, and using nautical convention also for ψ_L, the along and cross-course projection of the leeway are given by

$$w_{\parallel}^{(L)} = L\cos(\psi_e - \psi_L) = -\epsilon\, L\sin\delta, \tag{10a}$$

$$w_{\perp}^{(L)} = L\sin(\psi_e - \psi_L) = -\epsilon\, L\cos\delta. \tag{10b}$$

https://doi.org/10.5194/egusphere-2023-2060
Preprint. Discussion started: 16 November 2023

The simple relations on the r.h.s. of Eq. 10 follow from the similitude of the red and green-shaded triangles in Fig. 1. As δ typically is a small angle (cf. App. A), it is apparent that the cross component of the leeway, $w_\perp^{(L)}$, is the dominant one. Its sign is such that it is always downwind, see Fig. 1. If relevant, the Stokes' drift (van den Bremer and Breivik, 2018) could be treated akin to an ocean current, and one would obtain for its projections a couple of equations formally identical to Eq. 9.

Finally, the components of the effective flow ω advecting the vessel are

$$\omega_\parallel = w_\parallel + w_\parallel^{(L)}, \tag{11a}$$

$$\omega_\perp = w_\perp + w_\perp^{(L)}. \tag{11b}$$

Due to Eq. 10, both $\omega_\parallel$ and $\omega_\perp$ are functions of δ. We recall that the "cross" and "along" specifications refer to vessel course ψ_e, differing from vessel heading by the δ angle.

The graphical construction in Fig. 1 makes it clear that the SOG results from the vector sum of either STW and the current vector, or forward speed $\boldsymbol{F}$ and $\boldsymbol{\omega}$. Using the latter equality, together with the course assignment condition, and projecting along both $\hat{e}$ and $\hat{o}$, two scalar equations are obtained, namely:

$$S_g = F\cos(\delta) + \omega_\parallel, \tag{12a}$$

$$0 = -F\sin(\delta) + \omega_\perp, \tag{12b}$$

with S_g being the vessel's SOG. Eq. 12 are formally identical to those found in Mannarini and Carelli (2019) in presence of ocean currents only. This fact suggests the interpretation of ω as an effective current.

However, Eq. 12 alone is no more sufficient to determine the ocean current vector $\boldsymbol{w}$. In fact, it is mingled with the effect of wind through leeway, to form the effective flow ω (Eq. 11). This is why, in presence of strong winds, reconstruction of ocean currents from data of COG and HDG by simple inversion of Eq. 12 is challenging. This was indeed found by Le Goff et al. (2021) using Automatic Identification System (AIS) data across the Agulhas Current.

As it reduces the ship's velocity available along its course (Eq. 12a), the angle of attack δ plays a pivotal role in determining the SOG. However, in presence of an angle-dependent vessel velocity (Eq. 5a), δ is no more given by a simple algebraic equation corresponding to Eq. 12b as in Mannarini and Carelli (2019), but by a transcendental one:

$$\sin\delta = \frac{\omega_\perp(\delta, \delta_i(\delta))}{F(|\delta_i(\delta))|, |\delta_a(\delta)|)} \quad \Leftrightarrow \quad F \neq 0. \tag{13}$$

In fact, due to Eq. 2, the r.h.s. of Eq. 13 depends both explicitly and implicitly on δ. Just in the limiting case of null currents, Eq. 6, Eq. 10b and Eq. 12b collectively imply that

$$\delta = -\epsilon\alpha_L \tag{14}$$

However, in general, the actual value of the forward speed F is only determined once the δ angle is retrieved from Eq. 13. In App. A an efficient numerical approximation for the solution of the above equation with respect to δ is provided. Furthermore, Eq. 13 holds if and only if

$$|\omega_\perp| \leq F. \tag{15}$$

https://doi.org/10.5194/egusphere-2023-2060
Preprint. Discussion started: 16 November 2023

Should this not be the case, the vessels's forward speed would not balance the effective drift.

As F is always non-negative, Eq. (13) implies that $\mathrm{sgn}(\delta) = \mathrm{sgn}(\omega_\perp)$. In particular, in the case of an effective crossflow $\omega_\perp$ bearing, as in Fig. 1, to starboard, a counterclockwise change of vehicle heading ($\delta < 0$) is needed for keeping course.

Eq. 12 can be solved for the module S_g of the speed over ground, which reads

$$S_g = \omega_\parallel + \sqrt{F^2 - \omega_\perp^2}. \tag{16}$$

According to Eq. 16 the crossflow $\omega_\perp$ always reduces the SOG, as part of vehicle momentum must be spent for balancing the drift. The along-edge flow $\omega_\parallel$ (or "effective drag") may instead either increase or decrease SOG.

Finally, given that $\mathbf{S}_g = \mathrm{d}\boldsymbol{x}/\mathrm{d}t$, by taking the module of the left side, and approximating the r.h.s. (right-hand side) with its finite-difference quotient, the graph edge weight δt is computed as

$$\delta t = \frac{\delta x}{S_g}, \tag{17}$$

where δx is the edge length and S_g is given by Eq. 16. As the environmental fields determining the SOG are both space and time dependent, the weights δt are computed via the specific interpolation procedures in Sect. 2.3, and the shortest paths via the algorithms provided in Sect. 2.4.

From Eq. 17, it follows that the condition

$$S_g \geq 0 \tag{18}$$

should be checked in case the specific graph-search method used does not allow for use of negative edge weights (as is the case for the Dijkstra's algorithm, cf. Bertsekas (1998)). Violation of Eq. 18 may occur in presence of a strong counter-flow $\omega_\parallel$ along a specific graph edge, which weight must correspondingly be set to not-a-number.

The CO_2 emissions along a graph edge are given by

$$\delta CO_2 = \Gamma\,\delta t, \tag{19}$$

where $\Gamma = \Gamma(|\delta_i|, V_i; |\delta_a|, H_s, \chi)$ is the CO_2 emission rate of the specific vessel in presence of the actual meteo-marine conditions. Both δt and δCO_2 are used in the least-CO_2 algorithm introduced in Sect. 2.4.

2.2 Graph generation

The graph preparation is crucial for any graph-search method. The graph nodes determine the accessible locations of the domain, and the graph edges influence both the spatial smoothness of the routes and the representation of the environmental fields on the graph. Nodes and edges must be set keeping into account the presence of both the landmass and shallow waters.

The structure of the mesh is the most fundamental difference between a graph-search method (such as Dijkstra's one or A*) and dynamic programming. Indeed, a dynamic programming problem can be converted to a shortest path problem on a graph (Bertsekas, 1998)[Sect.2.1]. In the former, the nodes are organised along sections of variable amplitude corresponding to stages. In the latter, nodes can uniformly cover the whole domain. However, for both dynamic programming (Mason et al.,

https://doi.org/10.5194/egusphere-2023-2060
Preprint. Discussion started: 16 November 2023

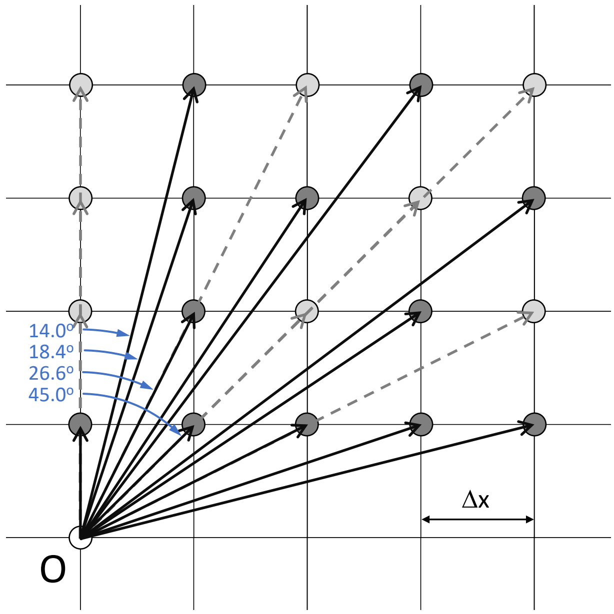

Figure 2. Graph stencil for $\nu = 4$. In VISIR-2, only the $N_{q1}(\nu)$ dark grey nodes (cf. Tab. 1) are connected to the origin, while in VISIR-1, all $\nu(\nu+1)$ nodes were connected. The angles resolved via the different edges are displayed in light blue.

2023) and graph-methods (Mannarini et al., 2019), the number of edges greatly affects the computational cost for computing a shortest path.

To efficiently deal with all these aspects, VISIR-2's graph preparation includes several updates with respect to its predecessor VISIR-1b, as detailed in the following sub-subsections.

2.2.1 No collinear edges

The first innovation regarding the graph is a pruning procedure for collinear edges.

In fact, some graph edges (both solid and dashed arrows in Fig. 2) may share the same orientation while differing for just the number of hops. In VISIR-1 multi-hop edges were admitted. However, in Mannarini et al. (2019), if crossing unsafe edges, they were pruned. In VISIR-2, just the shortest one among the collinear edges is kept. This corresponds to the solid arrows in Fig. 2. This way, the number N_{q1} of edges within a single quadrant is given by

$$N_{q1}(\nu) = 2\sum_{k=1}^{\nu} \varphi(k) \leq \nu(\nu+1) \tag{20}$$

where φ is Euler's Totient function and ν the maximum number of hops from a given node of the graph. Thus, the quantity right of the inequality represents the total number of edges of a quadrant, including collinear ones. Using Eq. 20, already at $\nu = 4$ more than one third of all edges get pruned, and, at $\nu = 10$, nearly half of them (cf. Tab. 1).

https://doi.org/10.5194/egusphere-2023-2060
Preprint. Discussion started: 16 November 2023

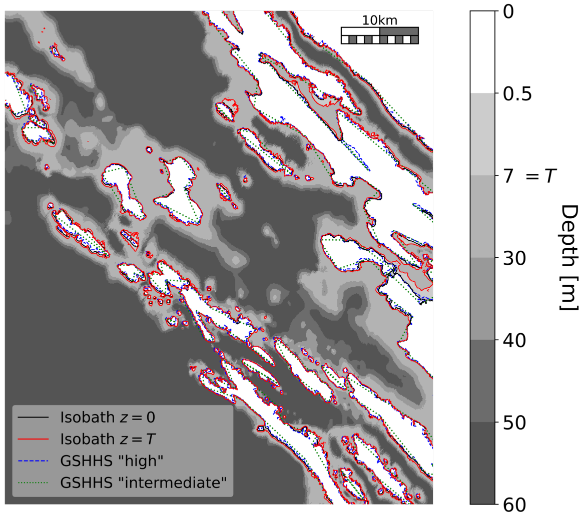

Figure 3. Bathymetry field from EMODnet represented in shades of grey, with contour lines at depths at $z = 0\mathrm{m}$ and $z = T$, where $T = 7\mathrm{m}$ is the vessel draught. Additionally, the GSHHS shoreline at two different spatial resolutions is included.

This benefits both the computer memory allocation and the computing time for the shortest path. The latter is linear in the number of edges, cf. Bertsekas (1998)[Sect.2.4.5], Mannarini et al. (2019). A further benefit of pruning collinear edges is a more faithful representation of the environmental conditions. In fact, the environmental field's values at the edge endpoints are averaged for estimating the edge weights (see Sect. 2.3). Thus, keeping just shorter edges avoids using a less spatially resolved information.

2.2.2 Bathymetry and draught

The minimal safety requirement is that navigation does not occur in shallow waters. It corresponds to the condition that vessel draught T does not exceed sea depth z at all graph edges used for the route computations. This is equivalent to a positive under keel clearance UKC = $z - T$. As explained later in Sect. 2.3.2, this can be checked by either evaluating the average UKC at the two edge nodes, or by interpolating it at the edge barycentre.

However, for some specific edge, UKC could still be positive and the edge cross the shoreline. This is avoided in VISIR by checking for mutual edge – shoreline crossings. Given the burden of this process, in VISIR-1b a procedure for restricting the check to inshore edges was introduced. In VISIR-2, on the other hand, as envisioned in Mannarini and Carelli (2019)[App.C], the process of searching for intersections is carried out using a K-dimensional Tree (KDT, Bentley (1975); Maneewongvatana and Mount (1999)). This is a means of indexing the graph edges via a spatial data structure which can effectively be queried for both nearest neighbours (coast proximity of nodes) and range queries (coast intersection of edges). In VISIR-2 the `scipy.spatial.KDTree` implementation was used[**].

[**] https://docs.scipy.org/doc/scipy/reference/

https://doi.org/10.5194/egusphere-2023-2060
Preprint. Discussion started: 16 November 2023

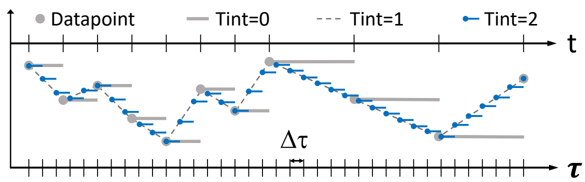

Figure 4. Time grid of VISIR-2. The upper horizontal axis (t) represents the coarse and uneven time resolution of the original environmental field. The lower horizontal axis corresponds to the fine and even time grid with resolution $\Delta\tau$ to which it is remapped.

Various bathymetric databases can be used by VISIR-2. For European seas, the EMODnet dataset[††] (1/16 arc-minute resolution or about 116 m) was used while, for a global coverage, the GEBCO_2022[‡‡] (15 arc-second resolution or about 463 m) is available.

2.2.3 Shoreline

The bathymetry dataset, if detailed enough, can even be used for deriving an approximation of the shoreline. From Fig. 3 it is seen that a "pseudo-shoreline" derived from the UKC=0 contour line of a fine-enough bathymetry (the EMODnet one) can effectively approximate an official shoreline (the GSHHG[§§] one, at the "high"-type resolution of 200 m).

Such pseudo-shoreline is the one used in VISIR-2 for checking the edge crossing condition specified in Sect. 2.2.2.

2.2.4 Graph edge orientation

For a given sea domain, a graph is typically computed once, and subsequently utilised for numerous different routes. However, in VISIR-1 graph edge orientation was recalculated every time a graph was utilised. Instead, in VISIR-2 edge orientation is computed just once, during graph generation, after which it is added to a companion file of the graph.

Furthermore, in the definition of the edge orientation, the nautical convention (due North, to-direction) is used in VISIR-2 graphs.

2.3 Edge weights

For computing the shortest paths, the graph edge weights are preliminarily needed. Due to Eq. 16 and Eq.5a-5b, they depend on both space- and time-dependent environmental fields, which information has to be remapped to the numerical grids of VISIR-2. This is done in a partly differently way than in VISIR-1, and is documented in what follows.

2.3.1 Time interpolation

The time at which edge weight are evaluated is key to the outcome of the routing algorithm.

[††] https://portal.emodnet-bathymetry.eu/
[‡‡] https://www.gebco.net/data_and_products/gridded_bathymetry_data/
[§§] https://www.ngdc.noaa.gov/mgg/shorelines/

https://doi.org/10.5194/egusphere-2023-2060
Preprint. Discussion started: 16 November 2023

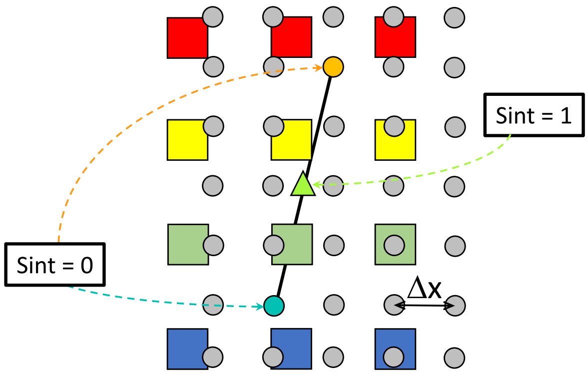

Figure 5. Spatial Interpolation in VISIR-2: The squares represent grid nodes of the original environmental field, and their colours correspond to the field value. The dots indicate the graph nodes, with head and tail of a specific edge coloured by field value. The triangle is positioned at the barycentre of the edge and its color indicates the average of the values at the edge's head and tail.

In Mannarini et al. (2019), to improve on coarse time resolution of the environmental field, a linear interpolation in time of the edge weight was introduced ("Tint = 1" option in Fig. 4). In VISIR-2 instead the environmental field values (grey dots) are preliminarily interpolated in time on a finer grid with $\Delta\tau$ spacing ("Tint = 2" or blue dots). Then, the edge weight at the nearest available timestep (floor function used, corresponding to the blue segments) is selected.

2.3.2 Space interpolation

The environmental fields and the graph grid may have different resolutions. Even though they were the same, the grid nodes may be staggered. Furthermore, it is necessary to define how to assign the environmental field values to the graph edges.

For these reasons, VISIR-2 first interpolates the environmental field to the graph grid nodes. Then, as shown in Fig. 5, two options are available: either averaging between the edge head and tail's values ("Sint = 0") or interpolating their values to the edge barycentre ("Sint = 1"). The latter is the default option, as it is computationally faster. Both options deliver the some outcome for the case of a linear field. Additionally, they benefit from pruning collinear edges (Sect. 2.2.1), as it leads to using edges with a smaller distance between head and tail and, thus, to a more accurate representation of the environmental fields.

Even before the spatial interpolation is performed, the so called "sea-over-land" extrapolation is applied to the marine fields. This step, which is needed for filling the gaps in the vicinity of the shoreline, is conceptually performed as in Mannarini et al. (2016a)[Fig.7]. Also, as the wave direction is a circular-periodic function, circular mean[¶¶] is applied ahead of interpolation by computing the arithmetic mean of its Cartesian components.

[¶¶]https://en.wikipedia.org/wiki/Circular_mean

https://doi.org/10.5194/egusphere-2023-2060
Preprint. Discussion started: 16 November 2023

2.4 Shortest path algorithms

A major improvement made possible by the Python coding of VISIR-2 is the availability of built-in, advanced data structures such as dictionaries, queues, and heaps. They are key in the efficient implementations of graph-search algorithms (Bertsekas, 1998). In particular, as data structures are used, Dijkstra's algorithm worst case performance can improve from quadratic, $\mathcal{O}(N^2)$, to linear-logarithmic, $\mathcal{O}(N \log N)$, where N is the number of graph nodes.

However, the original Dijkstra's algorithm (Dijkstra, 1959) considered static edge weights only. This was improved upon in VISIR-1 for dealing with dynamic edge weights. In Mannarini et al. (2016a), basing on Orda and Rom (1990), optimal routes under a first-in first-out (FIFO) hypothesis were obtained. In Mannarini et al. (2019) a validation of the dynamic algorithm was provided vs. the outcome of a path planning model based on partial differential equations (PDE).

However, that version of the shortest path algorithm could not be used with an optimisation objective differing from voyage duration. As one aims to compute e.g. least-CO_2 routes, the algorithm requires further generalisation. This has been addressed in VISIR-2 via the pseudocode provided in both Alg. 1 and Alg. 2. For its implementation in Python, we made use of a modified version of the `single_source_Dijkstra` function of the `networkX` Python library. The modification consisted in retrieving an edge weight at a specific time step. This is achieved via Alg. 2. Thereto, the $cost.at\_time$ pseudo-function represents a `networkX` method to access the edge weight information.

The shortest-distance and the least-time algorithm invoked for both motor- and sailboats are identical. Differences occur at post-processing level only, as different dynamical quantities (related to the marine conditions or the vessel kinematics) have to be evaluated along the optimal paths. Corresponding performance differences are evaluated in Sect. S1 of the Supplement.

2.4.1 non-FIFO

The FIFO-hypotesis by Orda and Rom (1990) enabled the authors to derive a shortest path algorithm in presence of dynamic edge weights, at the same computational complexity of an algorithm making use of static information only. However, if the rate of variation of an edge delay is large enough, they proved that an algorithm with a waiting time at the source node would deliver a faster path. The occurrence of such "non-FIFO" edges in a dynamic graph of a motorboat was investigated in Mannarini and Carelli (2019), finding that it was extremely rare (occurring for about 10^{-6} of the graph edges considered). For sailboats, this event can be more likely. This is due to the no-go-zone in their speed characteristics (Eq. 7, Fig. 7). Indeed, the unavailability of an edge can suddenly be lifted as the wind veers. However, under a FIFO-hypotesis, the algorithm would not wait for this improvement of the edge delay to occur. Rather, it would look for an alternative path avoiding the forbidden edge, potentially leading to a suboptimal path. In the case study of this paper, such a situation occurred for about $3 \cdot 10^{-4}$ of the sailboat routes, s. Sect. 5.2.2.

2.5 Vessel modeling

At the heart of the VISIR-2 kinematics of Sect. 2.1 are the vessel forward and transversal speed in a seaway, Eqs. 5a-5b. In what follows, such a vessel performance function is also termed as a "vessel model".

https://doi.org/10.5194/egusphere-2023-2060
Preprint. Discussion started: 16 November 2023

Algorithm 1 _DIJKSTRA_TDEP

Input: $(G, source, target, wT, Ntau, Dtau)$, respectively a `networkX` graph, *source* and *target* nodes, type of edge weight, maximum number of timesteps, and time resolution

Output: $(costs, paths)$, Two dictionaries keyed by node id: path costs from the source (e.g. cumulated CO_2), and corresponding optimal paths

$costs \leftarrow \{\}$
$seen \leftarrow \{source : 0\}$
$paths \leftarrow \{source : [source]\}$
 # $fringe$ is a min-priority queue of $(cost, node)$ tuples
$fringe \leftarrow heap()$
$fringe.push(0, source)$
while $fringe \neq \emptyset$ **do**
  $(d, v) \leftarrow fringe.pop()$
  if $v \in costs$ **then**
    # Already visited node
    $skip$
  end if
  $costs[v] \leftarrow d$
  if $v = target$ **and** $\forall n \in G.neigh(target), n \in seen$ **then**
    exit
  end if
  $t\_idx \leftarrow get\_time\_index(paths[v], d, wT, Ntau, Dtau)$
  # Iterate on v's forward-star
  for $(u, cost)$ in $G.succ(v)$ **do**
    # evaluate edge weight of wT type at time step t_idx
    $c \leftarrow cost.at\_time(t\_idx, wT)$
    $vu\_cost \leftarrow costs[v] + c$
    if $u \notin seen$ or $vu\_cost < seen[u]$ **then**
      $seen[u] \leftarrow vu\_cost$
      $fringe.push(vu\_cost, u)$
      $paths[u] \leftarrow paths[v] + [u]$
    end if
  end for
end while

https://doi.org/10.5194/egusphere-2023-2060
Preprint. Discussion started: 16 November 2023

Algorithm 2 GET_TIME_INDEX

Input: $(paths, d, wT, Ntau, Dtau)$, respectively a dictionary of paths, node costs, type of edge weight, maximum number of timesteps, and time resolution

Output: t_idx, the time step at which the costs d are realised along the $paths$

if $wT =$ "*time*" **then**
  $t\_idx \leftarrow min(Ntau, \lfloor d/Dtau \rfloor)$
else
  # compute $cTime$ cumulative time
  $cTime \leftarrow 0$
  $t\_idx \leftarrow 0$
  for $edge$ **in** $paths$ **do**
    # evaluate edge delay at time step t_idx
    $cTime \leftarrow cTime + edge.cost.at\_time(t\_idx,$"*time*"$)$
    $t\_idx \leftarrow min(Ntau, \lfloor time/Dtau \rfloor)$
  end for
end if

In VISIR-1 the forward speed resulted, for motorboats, from a semi-empirical parametrisation of resistances (Mannarini et al., 2016a) and, for sailboats, from polar diagrams (Mannarini et al., 2015). The transversal speed due to leeway had been neglected.

In VISIR-2 new vessel models were used, and two of them are presented in this paper: a ferry and a sailboat. The computational methods used to represent their speeds in a seaway are shortly described in Sect. 5.2.1-5.2.2. All methods provide the relevant kinematic quantities and/or the emission rates in correspondence of discrete values of the environmental variables. Such a "look-up table" (LUT) was then interpolated to provide VISIR-2 with a function to be evaluated at the actual environmental (wave, currents, or wind) conditions. Additional LUT can be used as well, and the relevant function for this part of the processing is `vesselModels_identify.py`.

The interpolating function either was a cubic spline (for sailboats) or the outcome of a neural network-based prediction scheme (for the ferry). The neural network features are provided in App. B. While the neural network generally demonstrated superior performance in fitting the LUT (see Sect. S2 of the Supplement), it provided unreliable data in extrapolation mode, as shown in Fig. 6-7. In contrast, the spline, when extrapolation was requested, returned the value at the boundary of the input data range.

2.5.1 Ferry

The ferry modelled in VISIR-2 was a medium-size Ro-Pax vessel which parameters are reported in Tab. 2. A vessel's seakeeping model was used at the ship simulator at the University of Zadar, as documented in Mannarini et al. (2021). Thereto, additional details about both the simulator and the vessel can be found. The simulator applied a forcing from wind-waves of

https://doi.org/10.5194/egusphere-2023-2060
Preprint. Discussion started: 16 November 2023

significant wave height H_s related to the local wind intensity V_i by

$$H_s[\mathrm{m}] = 0.0055 \cdot V_i[\mathrm{m/s}] + 0.0127 \cdot (V_i[\mathrm{m/s}])^2 \quad (21)$$

This relationship was derived by Farkas et al. (2016) for the wave climate of the middle Adriatic Sea. The simulator then recorded the resulting vessel speed, as well as some propulsion and emission-related quantities. Leeway could not be considered by the simulator. The post-processed data feeds the LUT to be then used for interpolating both the STW and CO_2 emission rate Γ as functions of: significant wave height H_s, relative wind-wave direction $\delta_a = \delta_i$, and fractional engine load χ. The results are displayed in Fig. 6.

In a given sea state, the sustained speed is determined by the parameter χ. For head seas ($\delta_a = 0°$) the STW is seen to decrease with H_s. The maximum speed loss varies from about 45% of the calm water speed at $\chi = 1$ to about 70% at $\chi = 0.7$ (Fig. 6.a). For $\chi = 0.7$, the STW sensitivity on H_s decreases from head ($\delta_a = 0°$) to following seas ($\delta_a = 180°$, Fig. 6.b). For this specific vessel, the increase in roll motion in beam seas, as discussed in Guedes Soares (1990), and its subsequent impact on speed loss, does not appear to be a relevant factor.

The Γ rate, which is in the order of 1 tCO_2 per hour, shows a shallow dependence on H_s (Fig. 6.c) while it is much more critically influenced by both χ and δ_a (Fig. 6.c.d).

2.5.2 Sailboat

Any sailboat described in terms of polars can in principle be used by VISIR-2. For the sake of the case study, a Bénétau First-367 was considered. Its hull and rigging features are given in Tab. 3.

The modelling of the sailboat STW was carried out by means of the WinDesign Velocity Prediction Program (VPP). The tool was documented in Claughton (1999, 2003) and references therein. The VPP is able to perform a four degrees of freedom analysis, taking into account a wide range of semi-empirical hydrodynamic and aerodynamic models. It solves an equilibrium problem by a modified multi-dimensional Newton-Raphson iteration scheme. The analysis considered the added resistance due to waves by means the so-called "Delft method" based on the Delft Systematic Yacht Hull Series (DSYHS). Besides, the tool allows to introduce response amplitude operators derived from other techniques as well, such as computational fluid dynamics. The wind-wave relationship was assumed to be given by Eq. 21. For each wind configuration (i.e., speed and direction) the optimal choice of sails set was considered. The main sail and the jib sail were considered for upwind conditions, otherwise the combination of main sail and spinnaker was used.

The outcome corresponds to Eq. 5 and is provided in Fig. 7. The no-go angle α_0 varies from 27 to 53°as the wind speed increases from 5 to 25 kn. At any true wind angle of attack δ_i, the forward velocity F increases with wind intensity, especially at lower magnitudes (Fig. 7.a). The peak boat speed is attained for broad reach ($\delta_i \approx 135°$). Leeway magnitude L instead is at largest for points of sail between the no-go zone ($\delta_i = \alpha_0$) and beam reach ($\delta_i = 90°$), see Fig. 7.b. As the point of sail transitions from the no-go zone to running conditions, the leeway angle α_L gradually reduces from 6 to 0°. This decrease follows a roughly linear pattern, as depicted in Fig. 7.c.

https://doi.org/10.5194/egusphere-2023-2060
Preprint. Discussion started: 16 November 2023

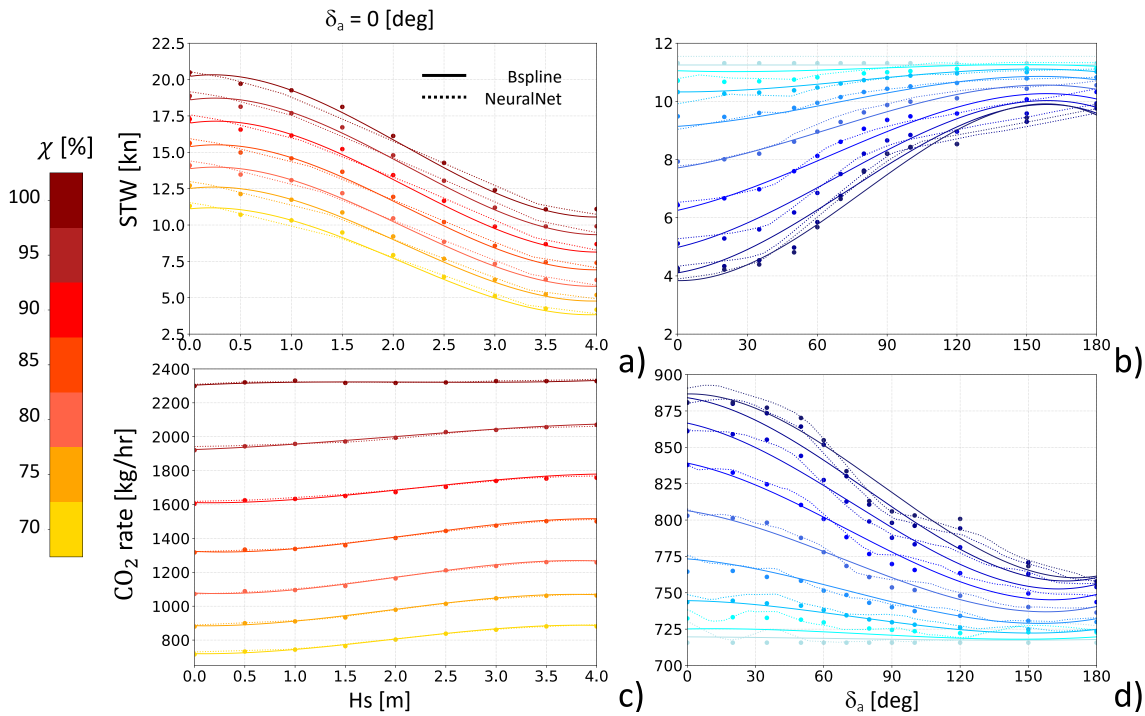

Figure 6. Ferry performance curve: In (a), STW is shown as a function of significant wave height H_s at a fixed relative angle $\delta_a = 0°$, with engine load χ indicated by the marker color. In (b), STW is plotted as a function of δ_a at a constant $\chi = 0.7$, with H_s represented by the colour variation. The lower panels (c, d) display the CO_2 emission rate (Γ) with similar dependencies as in panels (a, b). Markers correspond to the LUT values, solid lines represent the spline interpolation, and dashed lines indicate the neural network's output.

2.6 Visualisation

Further innovations brought in by VISIR-2 regard the visualisation of the dynamic environmental fields and the use of isolines.

To provide dynamic information via a static picture, the fields are rendered via concentric shells originating at the departure location. The shape of these shells is defined by isochrones. These are lines joining all sea locations which can be reached from the origin, upon sailing for a given amount of time. This way, the field is portrayed at the time step the vessel is supposed to be at that location. Isochrones bulge along gradients of vessel's speed. Such shells represent an evolution of the stripe-wise rendering introduced in VISIR-1.b (Mannarini and Carelli, 2019)[Fig.5]. The saved temporal dimensional of this plot type allows for its application in creating movies, where each frame corresponds to varying values of another variable, such as the departure date or engine load, see the Video Supplement of this paper.

In addition to isochrones, lines of equal distance from the route's origin (or: "isometres") and lines of equal amount of CO_2 emissions (or: "isopones") are also computed. The name isopone is related to energy consumption (the greek word means "equal effort") which, for an internal combustion engine, the CO_2 emission is proportional to. Isopones bulge against gradients of emissions. Isometres do not bulge, unless some obstruction (shoals, islands, landmass in general) prevents straight

https://doi.org/10.5194/egusphere-2023-2060
Preprint. Discussion started: 16 November 2023

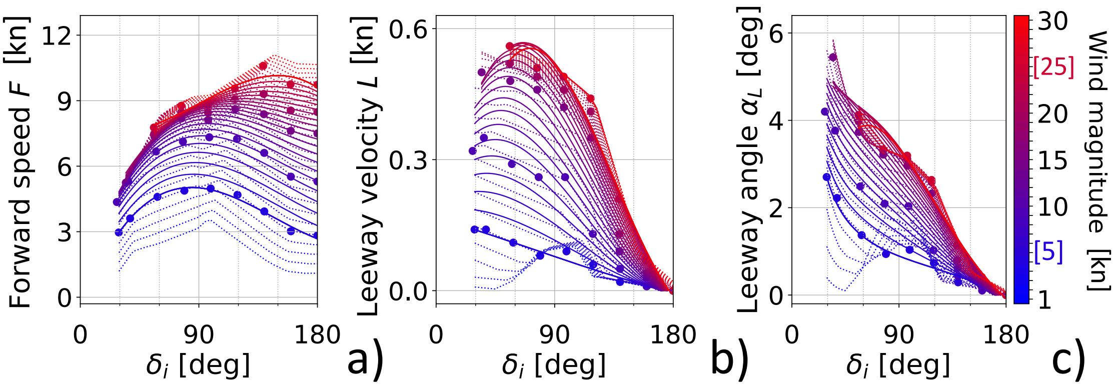

Figure 7. Sailboat performance curve: Forward speed F in (a) and leeway velocity L in (b) are both plotted against the true wind angle δ_i. (c) shows the leeway angle α_L obtained from Eq. 6. Marker and line colours represent wind magnitude V_i. Data start at $\delta_i = \alpha_0(V_i)$. Markers refer to the LUT, solid lines to spline interpolation, and dashed lines to the neural network's output. The colorbar also reports LUT's minimum and maximum values printed in blue and red, respectively.

navigation. Isochrones correspond to the reachability fronts used in a model based on the Level Set Equation (LSE) by Lolla (2016).

2.7 Code modularity

Software modularity has been greatly enhanced in VISIR-2. While in VISIR-1 modularity was limited to the graph preparation, which was detached from the main pipeline (Mannarini et al. (2016a)[Fig.8]), the VISIR-2 code is organised into many more software modules, as reported in Tab. 4. The modules can be run independently and can optionally save their outputs. Through the immediate availability of products from previously executed modules, this favours the research and development activities. For operational applications (such as GUTTA-VISIR) instead, the computational workflow can be streamlined by avoiding the saving of the intermediate results. VISIR-2 module names are Italian words. This is done for enhancing their distinctive capacity, cf. Wilson et al. (2014). More details on the individual modules can be found in the user manual, provided as part of the present release.

A preliminary graphical user interface (GUI) is also available. In the hereby released version of VISIR-2, it facilitates the ports selection from the World Port Index*** database.

VISIR-2 was developed on Mac OS Ventura (13.x). However, both path parameterisation and use of a virtual environment ensure portability, which was successfully tested for both Ubuntu 22.04.1 LTS and Windows 11, both on personal computers and two distinct high-performance computing (HPC) facilities.

***https://msi.nga.mil/Publications/WPI

https://doi.org/10.5194/egusphere-2023-2060
Preprint. Discussion started: 16 November 2023

3 Validation

Validation of a complex model, such as VISIR-2, is crucial. The code was built using specific runs of VISIR-1 as a reference. In turn, VISIR-1 was validated via comparison to benchmarks and extensive use in an operational service (Mannarini et al., 2016b). Comparisons of VISIR-1 to oracles for either a static wave field (Mannarini et al. (2016a)) or dynamic currents (Mannarini and Carelli (2019)) were provided in previous publications. Both tests referred to synthetic fields. In Mannarini et al. (2019), the routes computed in the presence of realistic dynamic wave fields were compared to the outcome of a PDE model. All these tests were performed also via VISIR-2, and their outcome is summarized in Tab. 5. For comparing to the outcome of such previous benchmarks, different from Sect. 2.2.1, collinear edges were retained in the graphs. The overall accuracy is quite satisfactory.

In the above-mentioned tests, the vessel STW did not depend on vector fields but just on scalar ones. Whenever the vector field of currents was present, it was combined with the STW, without affecting it. Thus, the new capacity VISIR-2 to deal with an angle-dependent vessel performance (cf. Eq. 5) needs to be demonstrated.

To this end, the openCPN model was used. It can compute sailboat routes without and with currents and is aware of the shoreline (but not bathymetry). For our tests, the same wind and sea currents fields used by openCPN were provided to VISIR-2 (details in Sect. 5.1), and the same sailboat polars were used by both models (without leeway though, which cannot be managed by openCPN). The VISIR-2 routes were computed on graphs of variable mesh resolution Δx and connectivity ν, keeping fixed the “path resolution” parameter ΔP which was introduced in Mannarini et al. (2019)[Eq.6]. Exemplary results are shown in Fig. 8, with related metrics provided in Tab. 6.

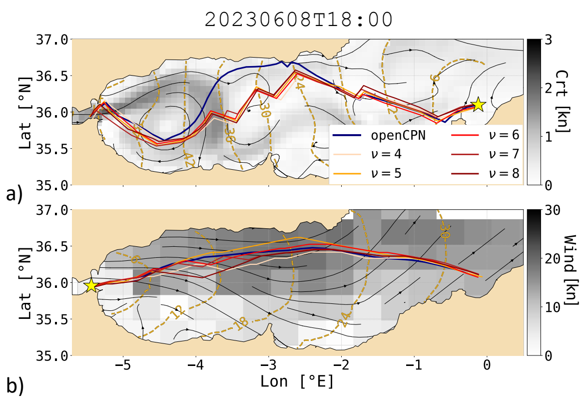

Figure 8. VISIR-2 routes with wind and currents vs. openCPN: Graphs of variable resolution, indexed by ν as shown in the legend, with a constant $\Delta P \sim 0.3°$. Field intensity is in grey tones, and the direction as black streamlines. Shell representation with isochrones in gold dashed lines and labels in hr. The openCPN solution is plotted as a navy line. Panels a) and b) refer to the West- and Eastbound voyage, respectively.

VISIR-2 routes are found to be topologically similar to openCPN ones but, for upwind sailing, they require a larger amount of tacking (Fig. 8.a). In the absence of currents, this usually implies a longer (between 6 and 10%) sailing time for VISIR-

https://doi.org/10.5194/egusphere-2023-2060
Preprint. Discussion started: 16 November 2023

2 routes. However, their duration decreases as the graph resolution is increased. It is also seen that the reduction ceases at $\nu = 7$, indicating that such a resolution is optimal for the given path length. This addresses the indication by Zis et al. (2020) about investigating the role of resolution in weather routing models. For a more in-depth discussion of this specific aspect, see Mannarini et al. (2019).

Downwind routes all divert Northwards because of stronger wind there. For these routes, the angular resolution is not a limiting factor and, starting from $\nu = 6$, VISIR-2 routes are even faster than openCPN' ones. As also currents are considered, VISIR-2 routes never lag more than 1.5% behind openCPN ones. Rather, as $\nu \geq 6$, they get faster for both up- and downwind experiments.

The differences in duration between openCPN and VISIR-2 could be ascribed to a number of factors, including: the way the wind field is interpolated in space and time, the role of time resolution, and the method to account for currents. We believe this requires a dedicated investigation, which falls beyond the scope of this paper.

Numerical tests have been integrated into this VISIR-2 release, covering the experiments listed in Tab. 5 and beyond. These tests can be run using the `Validazioni` module.

4 Computational performance

The computational performance of VISIR-2 was evaluated using tests conducted on a single node of the "juno" HPC facility at CMCC. This node was equipped with an Intel Xeon Platinum 8360Y processor, featuring 36 cores, each operating at a clock speed of 2.4 GHz, and boasting a per-node memory of 512 GB. Notably, parallelisation of the cores was not employed for these specific numerical experiments. Subsequently, our discussion narrows down to assessing the performance of the module dedicated to computing optimal routes ("`Tracce`") in its motorboat version.

In Fig. 9, we assess different variants of the shortest path algorithm: least-distance, least-time, and least-CO_2 . We differentiate between the core of these procedures, which focuses solely on computing the optimal sequence of graph nodes (referred to hereafter as the "Dijkstra" component), and the broader procedure ("total"), which also includes the computation of both marine and vessel dynamical information along the legs of the optimal paths.

The numerical tests utilise the number of degrees of freedom (DOF) for the shortest-path problem as the independent variable. This value is computed as $A \cdot N_\tau$, where A denotes the number of edges, and N_τ stands for the number of time steps of the fine grid (cf. Fig. 4). In the context of a sea-only edges graph, particularly in the case of a large graph (where border effects can safely be neglected), A can be represented as $4 \cdot N_{q1}(\nu)$, where N_{q1} is defined by Eq. 20. Random edge weights were generated for graphs with $\nu = 10$, resulting in a number of DOF ranging between 10^5 and 10^9. Each data point in Fig. 9 represents the average of three identical runs, which helps reduce the impact of fluctuating HPC usage by other users. Additionally, the computational performance of VISIR-2 is compared to that of VISIR-1b, as documented in Mannarini and Carelli (2019) [Tab.3, 'With T-interp'].

The primary finding is a confirmation of a power-law performance for all three optimisation objectives of VISIR-2: distance, route duration, and total CO_2 emissions. Remarkably, the curves appear nearly linear for the latter two algorithms (see

https://doi.org/10.5194/egusphere-2023-2060
Preprint. Discussion started: 16 November 2023

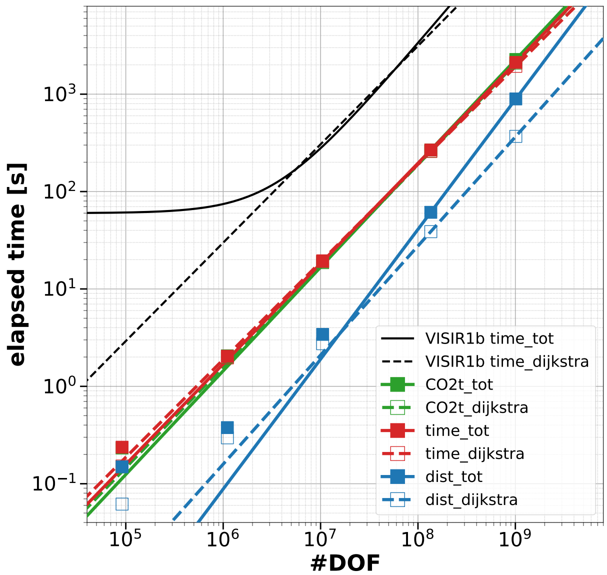

Figure 9. Profiling of computing time for the Tracce module (motorboat case). The independent variable is the #DOF in the graph. Markers refer to experimental data points and lines to least-square fits. Void markers and dashed lines refer to just the Dijkstra's component, while full markers and solid lines to the whole routines. The colours refer to the three alternative optimisation objectives, while black is used for VISIR-1.b results.

Tab. 7). Such a scaling is even better than the linear-logarithmic worst-case estimate for Dijkstra's algorithms (Bertsekas, 1998)[Sect.2.3.1]. Furthermore, this is not limited to just the Dijkstra components (as observed in VISIR-1.b), but extends to the entire procedure, encompassing the reconstruction of along-route variables. In addition to this enhanced scaling, VISIR-2 demonstrates an improved absolute computational performance within the explored DOF range. The performance gain is approximately a factor of 10 when compared to VISIR-1.b.

Digging deeper into the details, we observe that the least-distance procedure within VISIR-2, while exclusively dealing with static edge weights, exhibits a less favourable scaling behaviour, compared to both the least-time and least-CO_2 procedures. This is attributed to the post-processing phase, wherein along-route information has to be evaluated at the appropriate time step. Further development is needed to improve on this.

Lastly, it was found that peak memory allocation scales linearly across the entire explored range, averaging about 420B per DOF. This is about five times larger than in VISIR-1b and should be attributed to the `networkX` structures used for graph representation. However, the large memory availability at the HPC facility prevented a possible degradation of performance for the largest numerical experiments due to memory swapping. A reduction of the unit memory allocation by a factor of two should be feasible using single precision floating point format.

A more comprehensive outcome of the VISIR-2 code profiling, distinguishing also between the sailboat and the motorboat version of the `Tracce` module, is provided in the S1 section of the Supplement.

https://doi.org/10.5194/egusphere-2023-2060
Preprint. Discussion started: 16 November 2023

5 Case studies

A prior version of VISIR-2 has empowered both GUTTA-VISIR operational service, generating several million optimal routes within the Adriatic Sea over the span of a couple of years. In this section, we delve into outcomes stemming from deploying VISIR-2 in different European seas. While the environmental fields are elaborated upon in Sect. 5.1, the results are given in Sect. 5.2, distinguishing by ferry and sailboat.

5.1 Environmental fields

The fields used for the case studies include both static and dynamic fields. The only static one was the bathymetry, extracted from the EMODnet product of 2020[†††]. Its spatial resolution was 1/16 arcmin. The dynamic fields were the metocean conditions from both the European Centre for Medium-Range Weather Forecasts (ECMWF) and CMEMS. Analysis fields from the ECMWF high resolution Atmospheric Model, 10-day forecast (Set I - HRES) with 0.1° resolution[‡‡‡] were obtained. Both the u10m and v10m variables were used. From CMEMS, analyses of the sea state, corresponding to the MEDSEA_ANALYSISFORECAST_WAV_006_017 product, and of the sea surface circulation, MEDSEA_ANALYSISFORECAST_PHY_006_013, both with 1/24° resolution, were obtained. The wind-wave fields (vhm0_ww, vmdr_ww) and the Cartesian components (uo,vo) of the sea surface currents were used, respectively. Just for the comparison of VISIR-2 to openCPN (see Sect. 3), a lower resolution (0.4°, https://www.ecmwf.int/en/forecasts/datasets/open-data) ECMWF product and the RTOFS model output (1/12°, https://polar.ncep.noaa.gov/global/about/) for surface currents (p3049 and p3050 variables for U and V respectively) were used, respectively. Time resolution was three-hourly for both products.

5.2 Results

To showcase some of the novel features of VISIR-2, we present the outcomes of numerical experiments for both a ferry (as outlined in Sect. 5.2.1) and a sailboat (Sect. 5.2.2). All the results were generated using the interpolation options Sint=1 (as elaborated upon in Sect. 2.3.2) and Tint=2 (Sect. 2.3.1). These experiments considered the marine and atmospheric conditions prevailing in the Mediterranean Sea during the year 2022. Departures were scheduled from each port daily at 03:00 UTC. The relative savings (dQ) of a given quantity Q (such as the total CO_2 emissions throughout the journey or the duration of sailing) are computed concerning the geodetic route:

$$dQ = \frac{Q^{(\mathrm{opt})} - Q^{(\mathrm{gdt})}}{Q^{(\mathrm{gdt})}} \tag{22}$$

5.2.1 Ferry

The chosen domain lies at the border between the Provençal Basin and the Ligurian Sea. Its sea state is significantly influenced by the Mistral, a cold northwesterly wind that eventually affects much of the Mediterranean region during the winter months.

[†††] https://emodnet.ec.europa.eu/en/bathymetry
[‡‡‡] https://www.ecmwf.int/en/forecasts/datasets/set-i#I-i-a_fc

https://doi.org/10.5194/egusphere-2023-2060
Preprint. Discussion started: 16 November 2023

The circulation within the domain is characterized by the southwest-bound Liguro-Provençal current and the associated eddies. (Schroeder and Chiggiato, 2022).

We conducted numerical experiments using VISIR-2 with a graph resolution given by $(\nu, 1/\Delta x) = (4, 12/°)$, resulting in 2,768 nodes and 114,836 edges within the selected domain. The time grid resolution was set at $\Delta\tau = 30\text{min}$ and $N_\tau = 40$. A single iteration ($k = 1$) of equation Eq. A1 was performed. The ferry engine load factor χ was varied to encompass values of 70, 80, 90, and 100% of the installed engine power. For each day, both route orientations, with and without considering currents, were taken into account. This led to a total of 5,840 numerical experiments. The computation time for each route was approximately 4 min, with the edge weight and shortest path calculations consuming around 30 sec.

In Fig. 10.a an illustrative route is shown during a Mistral event. As the ferry navigates against the wind, both its speed loss and CO_2 emission rate reach their maximum levels (cf. Fig. 6.b.d). Consequently, the least-CO_2 algorithm calculates a detour into a calmer sea region where the combined benefits of improved sustained speed and reduced CO_2 emissions compensate for the longer path's costs. Additionally, the detour skips a southbound meander of the Liguro-Provençal current, which would otherwise diminish the ferry's SOG. An evident recession of the isochrone for 18hr since departure can be noticed. It is due to the reduction in SOG resulting from the combined influence of waves and cross-currents, cf. Eq. 16. For this specific departure date and time, the overall reduction in CO_2 emissions, in comparison to the shortest-distance route, exceeds 33$\%$.

Fig. 10.b illustrates that the magnitude of the related spatial diversion is merely intermediate, compared to the rest of 2022. Particularly during the winter months, the prevailing diversion is seen to occur towards the Ligurian Sea. Notably, VISIR-2 even computed a diversion to the East of Corsica, which is documented in Sect. S3.1 of the Supplement. In the supplementary video accompanying this manuscript, all the 2022 routes between Port Torres and Toulon are rendered, along with relevant environmental data fields.

To delve deeper into the statistical distribution of relative CO_2 savings defined as in Eq. 22, Fig. 11.a provides a comparison with both the average significant wave height $\langle H_s^{(\text{gdt})} \rangle$ and absolute wave angle of attack $\langle |\delta_a^{(\text{gdt})}| \rangle$ along the shortest-distance route. Firstly, it should be noted that an increase in wave height can lead to either substantial or minimal CO_2 emission savings. This outcome depends on whether the prevailing wave direction is opposing or aligned with the vessel's heading. When focusing on routes with a relative CO_2 saving of at least 2$\%$, it is seen that they mostly refer to either beam or head seas along the geodetic route. This corresponds to elevated speed loss and subsequent higher emissions, as reported in Fig. 6b.d. This subset of routes shows a trend of larger savings in rougher sea states. Conversely, when encountering following seas with even higher H_s, savings remain below 1$\%$. This is due to both a smaller speed reduction and a lower CO_2 emission rate. The counts of routes surpassing the 2$\%$ saving threshold accounts for nearly one-tenth of the total routes, the ones above the 10$\%$ threshold, represent about 1/30th of the cases. This implies that, for the given ferry and the specified route, double-digit savings can be anticipated for more than ten calendar days per year.

The analysis of the CO_2 savings distribution can be conducted by also considering the role of the engine load factor χ, as depicted in Fig. 11.b. The distribution curves exhibit a bi-exponential shape, with the larger of the two decay lengths (d_2) inversely proportional to the magnitude of χ, cf. Tab. 9. This relationship is connected to the observation of reduced speed

https://doi.org/10.5194/egusphere-2023-2060
Preprint. Discussion started: 16 November 2023

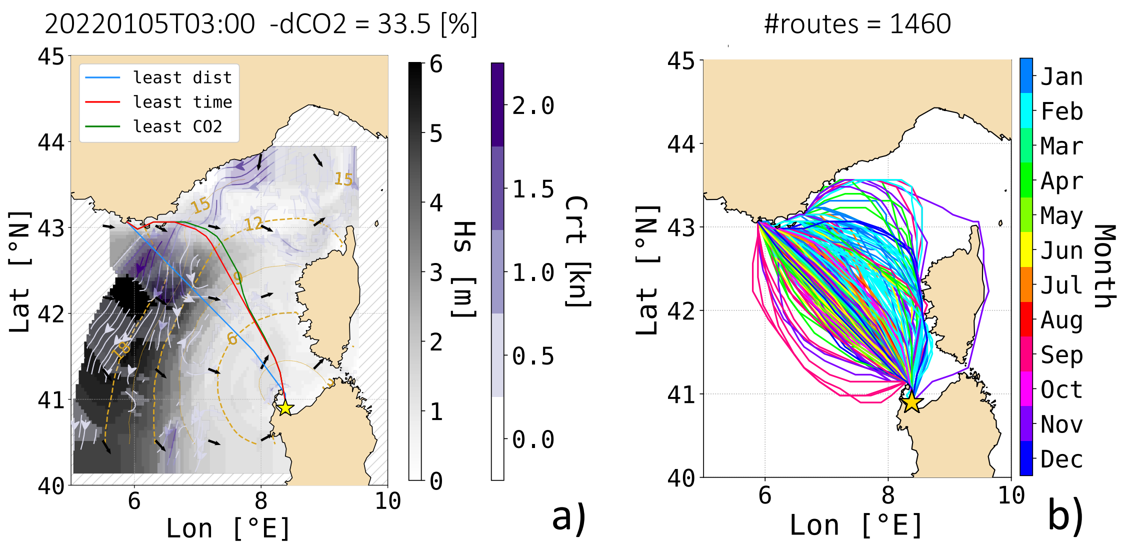

Figure 10. Ferry's optimal routes between ITPTO and FRTLN: a) For the specified departure date and time, the least-CO_2 route is shown in green, the least-time route in red, and the shortest-distance route in blue. The H_s field is displayed in shades of grey with black arrows, while the currents are depicted in purple tones with white streamlines. Environmental field values are not provided for the etched area. Additionally, isochrones of the CO_2 -optimal route are shown at 3-hourly intervals. The engine load was $\chi = 0.7$. b) A bundle of all northbound CO_2 -optimal routes (for $\chi = [0.7, 0.8, 0.9, 1.0]$) is presented, with the line colour indicating the departure month.

loss at higher χ as rougher sea conditions are experienced, which was already noted in the characteristics of this vessel in Sect. 5.2.1. The distribution's tail can extend to values ranging between 25 and 50%, depending on the specific value of χ.

Relative CO_2 savings, broken down by sailing direction and considering the presence or absence of currents, are detailed in Tab. 8. The average savings range from 0.7% (0.9% when considering sea currents) to 2.0% (2.5%), where the larger values are achieved at the lower χ values. It is confirmed that the savings are more substantial on the route that navigates against the Mistral wind (from Porto Torres to Toulon). However, the relative savings amplify when currents are taken into account, and this effect is particularly noticeable for the routes sailing in the downwind direction.

5.2.2 Sailboat

The chosen area lies in the southern Aegean Sea, along a route connecting Greece (Monemvasia) and Turkey (Marmaris). This region traverses one of the most archipelagic zones within the Mediterranean Sea, which is historically significant as the origin of the term "archipelago". The sea conditions in this area are significantly influenced by the Meltemi, a prevailing northerly wind, particularly during the summer season. Such an "Etesian" weather pattern can extend its influence across a substantial portion of the Levantine basin (Schroeder and Chiggiato, 2022). On the eastern side of the domain, the circulation is characterised by the westbound Asia Minor Current, while on its western flank, two prominent cyclonic structures separated by the West-Cretan anticyclonic gyre are usually found. (Theocharis et al., 1999).

https://doi.org/10.5194/egusphere-2023-2060
Preprint. Discussion started: 16 November 2023

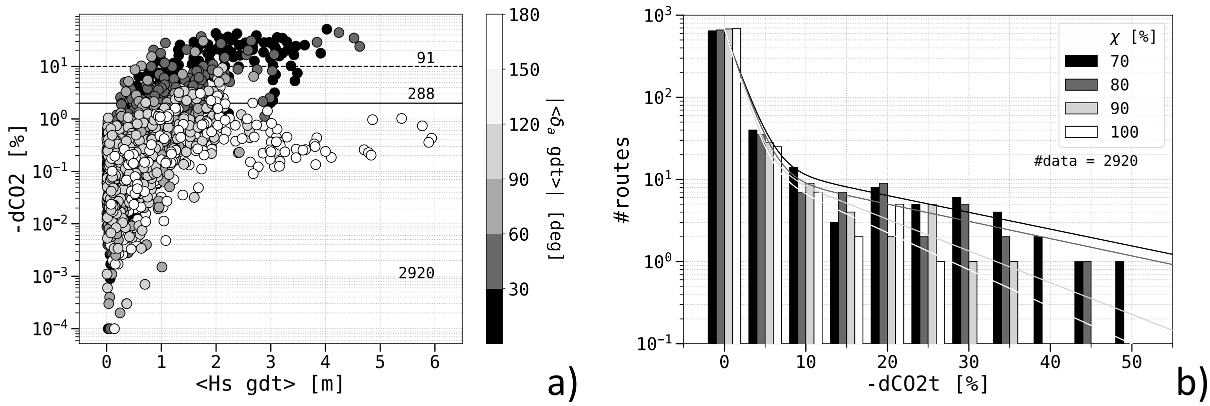

Figure 11. Metrics relative to routes of Fig. 10, pooled on sailing directions and χ. a) Relative savings, with marker's grey shade representing the mean angle of attack along the geodetic. The total number of routes, those with relative CO_2 savings above 2% (solid line) and 10% (dashed), are also provided; b) Distributions of the CO_2 savings for each χ value, with fitted bi-exponential functions as in Tab. 9. Each set of four columns pertains to a bin centred on the nearest tick mark and spanning a width of 5%.

We performed numerical experiments with VISIR-2, with a graph resolution of $(\nu, 1/\Delta x) = (5, 15/°)$, leading to 2,874 nodes and 156,162 edges in the selected domain. The resolution of the time grid was $\Delta\tau = 30$ min. Furthermore, $N_\tau = 120$ time steps of the environmental fields and $k = 2$ iterations for Eq. A1 were used. A First-367 sailboat was selected. For each day, both route orientations, and all possible combinations of wind, current, and leeway were considered. This implied a total of 2,920 numerical experiments. Each route required a total computing time of about 7 min, of which the edge weight and shortest path computation amounted to 4 min, mainly spent in the edge weight computation. The excess duration in comparison to the motorboat's case study is attributed to both a higher value of N_τ and the additional time required for accounting for the exclusion of the no-go zone of the sailboat shown in Fig. 7.

In Fig. 12.a, a sailboat route is depicted for a specific departure date, superimposed on the wind and sea current patterns. Both the geodetic and optimal routes appropriately steer clear of both continental and insular landmasses, with the time-optimal route opting for a more extensive detour. This adjustment is aimed at harnessing more favourable winds and circumventing unfavourable or cross currents, culminating in a remarkable 15.7% reduction in route duration.

Moving to Fig. 12.b, the collective set or "bundle" of eastbound routes is presented. Unlike the ferry routes showcased in Fig. 10.b, it proves more challenging to discern a distinct seasonal pattern for the diversions of the sailboat routes, although some of the more substantial deviations continue to manifest during the winter months. The corresponding return routes are shown in Sect. S4.2 of the Supplement, confirming this trend. However, the most significant winter diversions are observed to the north of the shortest-distance route. The bundles indicate that accounting also for currents leads to a more expansive set of optimal routes.

In just one case, the least-time route was found not be faster than the geodetic route. As shown in Sect. S3.2 of the Supplement, in this case reaching a graph edge later allowed for an earlier exit. It thus indicates a potentially non-FIFO situation (see

https://doi.org/10.5194/egusphere-2023-2060
Preprint. Discussion started: 16 November 2023

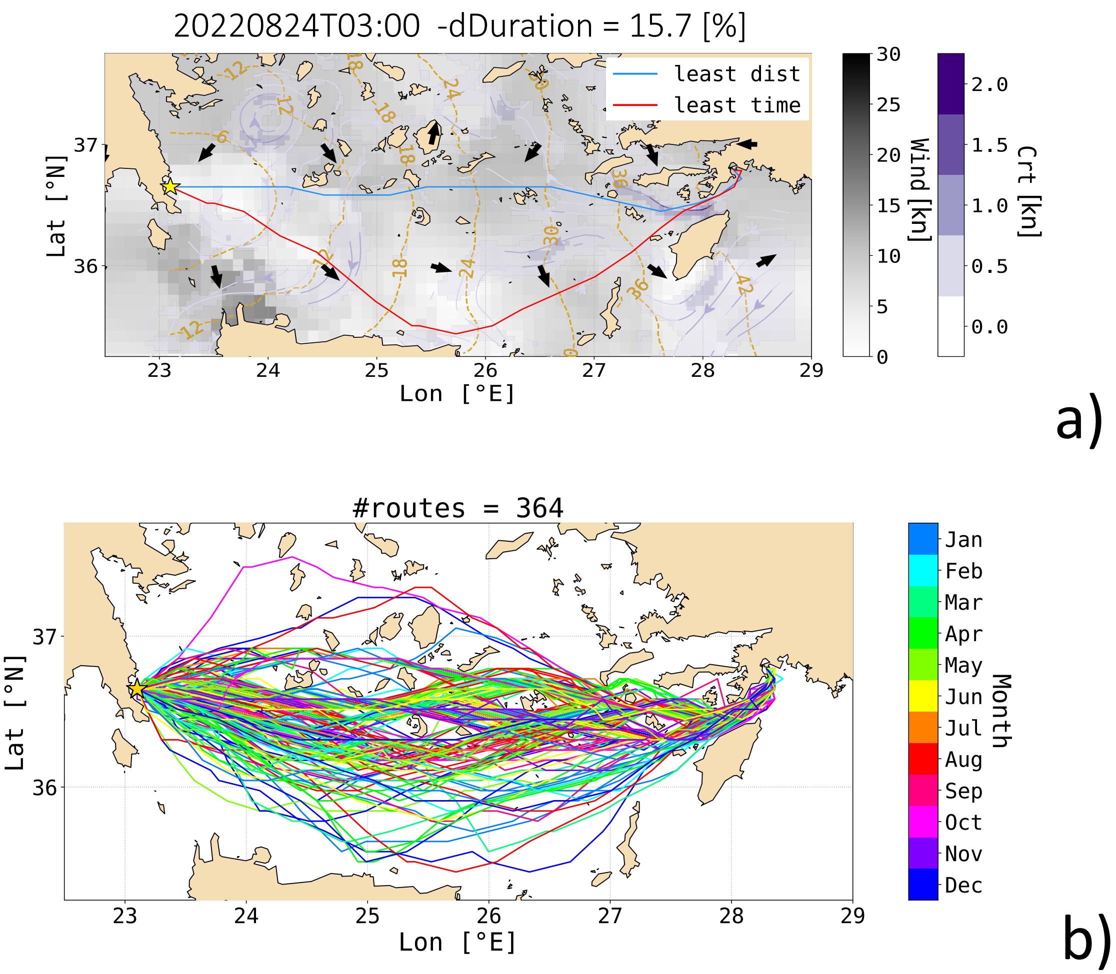

Figure 12. Sailboat's optimal routes between GRMON and TRMRM: a) For the specified departure date and time, the least-time route is depicted in red, and the shortest-distance one in blue. The wind field is represented in shades of grey with black arrows, while the currents are shown in purple tones with white streamlines. Additionally, isochrones of the time-optimal route are displayed at 3-hourly intervals. b) A bundle of all eastbound time-optimal routes is presented, with the line colour indicating the departure month.

Sect. 2.4.1). In the video supplement, all the 2022's routes between Monemvasia and Marmaris as well as related environmental fields are provided.

A statistical evaluation of the time savings resulting from the optimisation process for sailboat routes is illustrated in Fig. 13.a. Thereto, Eq. 22 is employed to assess both the path length and duration relative savings. While the $-dT$ savings are generally proportional to the path lengthening dL, the most substantial savings manifest under nearly upwind conditions along the geodetic route, i.e. where $\langle|\delta_i^{(\mathrm{gdt})}|\rangle \sim \alpha_0$. This is understandable, as reduced sustained speeds and extended edge sailing times occur when wind originates from sectors close to the no-go zone, as depicted in Fig. 7.a. However, it is worth noting

https://doi.org/10.5194/egusphere-2023-2060
Preprint. Discussion started: 16 November 2023

that, under excessively weak or consistently sustained upwind conditions, a sailboat route might become unfeasible. A quantitative overview of such "failed" routes is provided in Tab. 10. It is evident that, thanks to the spatial diversions introduced, the likelihood of an optimal route failing, compared to the geodetic one, is reduced by a factor of approximately 100.

In Fig. 13.b of the impact of currents and leeway is assessed. The effect of currents results in a change in duration, in either direction, of up to about 5% when compared to routes affected solely by the wind. Categorising the data based on sailing direction (as presented in Sect. S5 in Supplement), currents primarily contribute to shorter route durations for westbound courses (benefiting from the Asia Minor current). Conversely, they result in extended durations for eastbound routes where, to the North of the island of Rhodes, there is no alternative to sailing against the current.

Turning to leeway, it consistently extends the duration of routes. Particularly, as indicated in the Supplement, when facing upwind conditions (more likely for westbound routes), the speed loss is exacerbated due to a higher leeway velocity (refer to Fig. 7.b). This is indeed consistent with our earlier observation in Sect. 2.1 that the impact of leeway is mainly provided by its cross-course component, which invariably decreases the vessel's SOG. Notably, the longitudinal component is smaller than the cross-one by a factor of $\tan\delta$, cf. Eq. 17. With δ estimated from Eq. 14 and Fig. 7.c to fall within a range of a few degrees, the along-edge projection of leeway, $w_{\parallel}^{(L)}$, measures approximately one-tenth of the transversal one, $w_{\perp}^{(L)}$.

When both effects, currents and leeway, are considered together, the distribution of duration changes in comparison to wind-only routes resembles the distribution for wind and currents. However, due to the impact of leeway, it is slightly skewed towards longer durations.

Finally in Tab. 10 time savings averaged throughout the year are presented. These savings are further categorised based on the direction of sailing and the specific combination of effects, including wind, currents, and leeway. The impact of the sea current can be especially appreciated for the westbound routes (TRMRM - GRMON). This should be ascribed to the Asia Minor current leading to significantly larger average savings with respect to the wind-only routes. However, since this sailing direction also involves prevailing upwind conditions (s. Fig.S16.a of Supplement), the adverse effect of leeway reduces the potential savings attributed to the currents. In contrast, for the GRMON-TRMRM direction, the additional time gains resulting from considering the sea current, which is largely unfavourable, are more modest. Nevertheless, when accounting for leeway, a larger average time saving relative to the geodetic routes is realised. This could be attributed to the prevailing downwind conditions (Fig.S17.a of Supplement), which offer flexibility for the shortest path algorithm to select courses that minimise speed loss due to leeway along the geodetic route. This situation stands in contrast to most westbound routes, which navigate in proximity to the nogo-zone, limiting the available feasible headings. The count of failed routes reported in Tab. 10 is also consistent with prevailing upwind conditions along the TRMRM - GRMON routes.

The distinct impacts of currents or leeway typically lead to fractional percentage enhancements in travel time compared to optimal routes considering wind alone (refer to Tab. 10). However, these improvements can often prove sufficient to gain a competitive edge in sailboat races.

https://doi.org/10.5194/egusphere-2023-2060
Preprint. Discussion started: 16 November 2023

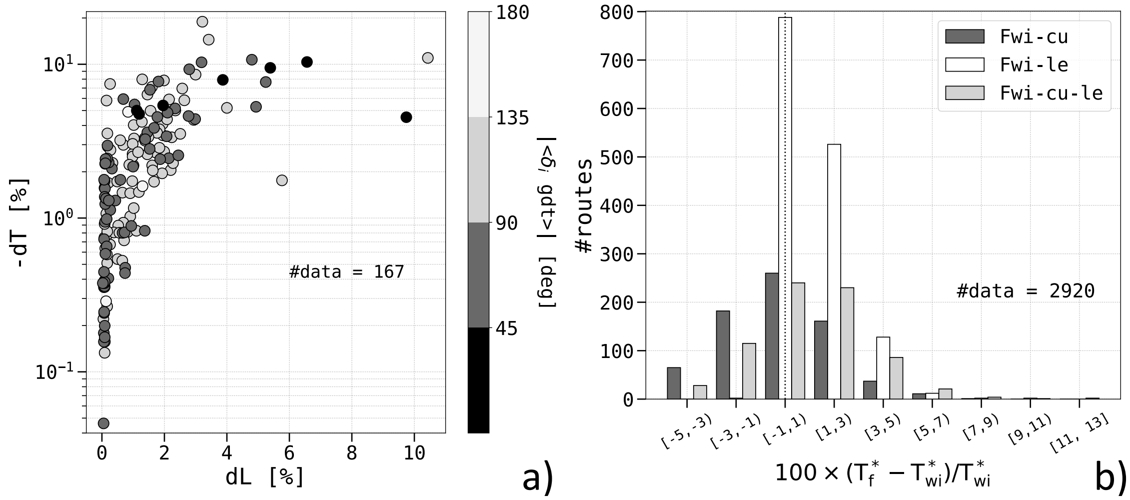

Figure 13. Metrics of the sailboat's optimal routes. a) Scatter plot of duration relative savings $-dT$ vs. relative lengthening dL. The marker shape represents the average angle of attack of wind $|\langle\delta_i^{(\mathrm{gdt})}\rangle|$ along the geodetic. The #data is consistent with the first row in Tab. 10. b) Histograms of relative route duration T_f, with forcing combination f defined by the column colour, with respect to the duration T_{wi} of the wind-only optimal routes.

6 Conclusions

This manuscript presented the development of VISIR-2: a modular, validated, and portable model for ship weather routing. It provides a consistent framework for both motor- and sailboats by accounting for dynamic environmental fields such as waves, currents, and wind. The model can compute optimal ship routes even in complex and archipelagic domains. It provides, for vessels with an angle-dependent performance curve, an improved level of accuracy in the velocity composition with sea currents. It is found that heading and course differ by an angle of attack, which is given by the solution of a transcendental equation (Eq. 13) involving an effective flow being the vector sum of currents and leeway velocity. A computationally inexpensive iterative solution has been devised (App. A). Furthermore, a variant of the Dijkstra's algorithm is introduced and used, which can minimise not just the CO_2 emissions but any figure of merit depending on dynamic edge weights, cf. Alg. 1.

The validation of VISIR-2 included comparisons to reference models and two inter-comparison exercises (against both a PDE-based model and the openCPN package). Different from the few available ship weather routing packages or services, the VISIR-2 software is accompanied by comprehensive documentation, making it suitable for community use.

Also, the computational performance of the VISIR-2 shortest path module displayed a significant enhancement compared to its predecessor, VISIR-1 (Sect. 4). A quasi-linear scaling with problem complexity was demonstrated up to one billion DOF. The robustness of VISIR-2 was demonstrated across thousands of flawless route computations.

Two case studies with VISIR-2, based on realistic vessel seakeeping models, were documented in this paper.

https://doi.org/10.5194/egusphere-2023-2060
Preprint. Discussion started: 16 November 2023

From nearly six thousand routes of a 125-meter-long ferry, computed considering both waves and currents in the North-Western Mediterranean, average CO_2 savings between 0.9 and 2.5%, depending on the engine load, were found. The distribution of the savings was bi-exponential, with the longer decay length becoming more pronounced at lower engine loads. This implied in particular that two-digit CO_2 savings were possible for more than ten days annually. This sheds new light on the underlying factors contributing to the variability observed in the role of weather routing, as reported in previous review studies (Bouman et al., 2017; Bullock et al., 2020). Furthermore, our findings bear significance for both the environmental impact of greenhouse gas emissions and the financial considerations within the EU-ETS.

From close to three thousand routes of an 11-meter sailboat, within the Southern Aegean Sea, accounting for both wind and currents, an average time reduction of approximately 3% was observed. When considering currents as a factor, the duration of optimal routes experienced alterations significant enough to potentially confer a competitive advantage in races. Additionally, disregarding the role of leeway would lead to an incorrect underestimation of the optimal routes' duration. This is, to our knowledge, the first of its kind assessment for sailboats, encompassing the influence of both currents and leeway. It is relevant for both sailboat racing and use of wind in assisting propulsion of motor vessels.

For both the ferry and the sailboat, the most substantial savings, whether in terms of CO_2 emissions or sailing time, were achieved by circumventing upwind sailing conditions along the direct route between the departure and arrival ports.

Given its open-source nature, validated results, and numerical stability, VISIR-2 can hold great utility across various fields. It can serve as a tool for inter-comparison studies and creation of baseline numerical experiments, as indicated by Zis et al. (2020). The fact that both motorboats and sailboats are treated equally will make VISIR-2 suitable for use in weather routing of vessels with wind-assisted propulsion. Moreover, VISIR-2 can be utilised by regulatory bodies to inform policies on shipping. Specifically, by narrowing the uncertainty about the potential of weather routing for CO_2 emission reduction (Bullock et al., 2020). For instance, by evaluating changes in Fig. 11.b, it becomes possible to characterise the joint potential of sea domains and vessel types for GHG emission savings. This concept also aligns with the idea of a "green corridor of shipping", as envisioned by both the Clydebank Declaration (gov.uk, 2021) and the United States' Department of State (DoS, 2022). In these initiatives, weather routing, and VISIR-2 in particular, thanks to the generality of algorithm Alg. 1, could play a crucial role in minimizing the consumption of costly zero-carbon fuel. Furthermore, VISIR-2 could be used to generate a dataset of optimal routes for the training of artificial intelligence systems for autonomous vessels (Li and Yang, 2023), surpassing the shortcomings of using AIS tracks, which include incomplete coverage (Filipiak et al., 2020). Finally, we note that, as an open-source software, VISIR-2 can even have educational purposes, providing training opportunities for ship officials and maritime surveillance authorities, as well as for beginner sailors.

There are several possible avenues for future improvements of VISIR-2. First, as mentioned in Sect. 4, some computational performance improvements for the least-distance procedure should be feasible. In applications where large domains, hyper-resolution, or multiple input environmental fields are required, it will be necessary to devise a solution that effectively reduces the computer's memory allocation. To further enhance modularity of VISIR-2, future developments can focus on object-oriented programming principles. This will enable greater flexibility, collaboration and maintenance, as well as integration with other models or systems.

https://doi.org/10.5194/egusphere-2023-2060
Preprint. Discussion started: 16 November 2023

Passing to ocean engineering aspects, dynamic safety constraints, such as vessel intact stability, voluntary speed reduction (Mannarini et al., 2016a), considerations for slamming, green water, lateral acceleration (Vettor and Guedes Soares, 2016), and passenger comfort, as highlighted by Carchen et al. (2021), or vessel performance in the presence of cross-seas could be integrated. VISIR-2's readiness for wind-assisted ship propulsion hinges on the availability of an appropriate vessel performance curve that accounts for both wave and wind conditions.

Future algorithmic work could address, for instance: efficient algorithms for given-duration least-CO_2 routes; incorporating multi-objective optimisation techniques, as done e.g. in Sidoti et al. (2017); consideration of tacking time and motor-assistance for sailboats.

In terms of environmental data, VISIR-2 currently operates under the assumption of having perfect knowledge of metocean conditions, which is provided through forecast fields for shorter voyages or analysis fields for longer ones. The latter corresponds to retracked routes as discussed in Mason et al. (2023). However, for real-time applications during extended voyages, it is essential to incorporate adaptive routing strategies. This entails using the latest forecasts to execute re-routing as needed.

Code availability. Source code of VISIR-2 is available at https://zenodo.org/records/8305527, DOI: 10.5281/zenodo.8305527. The distribution includes a user manual.

Data availability. Raw data: input datasets and graphs used for the route computations are available at https://zenodo.org/records/8321216, DOI: 10.5281/zenodo.8321216; Intermediate data products: routes for producing figures and tables in Sect. 5 are available at https://zenodo.org/records/8233874, DOI: 10.5281/zenodo.8233874.

Video supplement. Videos for this manuscript are available at https://av.tib.eu/media/62912 and https://av.tib.eu/media/62913

Appendix A: Angle of attack

The angle δ between ship's heading and course is obtained from the transcendental equation Eq. 13. Its solution can be approximated by the iteration:

$$\begin{aligned} \delta^{(0)} &= 0 \\ \delta^{(k)} &= h(\delta^{(k-1)}) \quad \text{for} \quad k = 1, 2, \ldots \end{aligned} \tag{A1}$$

where k is the number of iterations of the function

$$h(x) = \arcsin\left(\frac{\omega_\perp(\delta = x, \delta_i = x - \gamma)}{F(|x - \gamma|)}\right) \tag{A2}$$

https://doi.org/10.5194/egusphere-2023-2060
Preprint. Discussion started: 16 November 2023

with γ being a constant resulting from the use of Eq. 2. The $k = 1$ case correspond to the solution provided in Mannarini and Carelli (2019).

Both Eq. 13 and Eq. A1 were evaluated for a sailboat as in Sect. 5.2.2 using environmental conditions (wind, currents) for a domain in the central Adriatic Sea. 11 hourly time steps and 18,474 edges from a graph with $(\nu, 1/\Delta x) = (4, 12/°)$ were considered, resulting in a total of about $2 \cdot 10^5$ edge weight values. The iterative solution from Eq. A1 was compared to the roots of Eq. 13 found via the `scipy.optimize.root` solver, using as an initial guess the $\delta^{(1)}$ solution of Eq. A1 (see `velocity_eval.py` function in the VISIR-2 code). In what follows, the numerical solution from the solver is termed as "exact". The benefit of the approximated solution Eq. A1 is that it can easily be parallelised on all graph arcs, while this is not possible for the exact solution which processes one arc at time.

The outcome for a sailboat is provided in Fig. A1.a. It is seen that the iterative approximation departs from the exact solution for δ angles larger than about 5°. Such departures are mainly related to the effective cross-flow $\omega_\perp$ (marker colour, determining the elongation from the origin). However, it is just a tiny fraction of the edges presenting such departures, so that the R^2 correlation coefficient between the exact solution and its approximation is almost identical to 1 for any $k > 0$, as shown in Fig. A1.b.

The case $k = 0$ corresponds to neglecting the loss of ships' momentum to balance the effective cross flow of Eq. 11b. Therefore, it wrongly underestimates the sailing times. For the First-367 sailboat under consideration here, the $k = 1$ solution leads to a slope about 5% off. Already for $k = 2$ the correct slope is achieved within an error of 2‰. For the ferry, the $k = 1$ iteration is sufficient to reach a 1% accuracy, see Sect. S6.1 in Supplement. This could be due to the ferry having a smoother angular dependence than the sailboat's one, as seen from Fig. 6.b and Fig. 7.a. Finally, in Sect. S6.2 of the Supplement, evidence of the validation of the exact solution in the absence of currents, Eq. 14, is also provided.

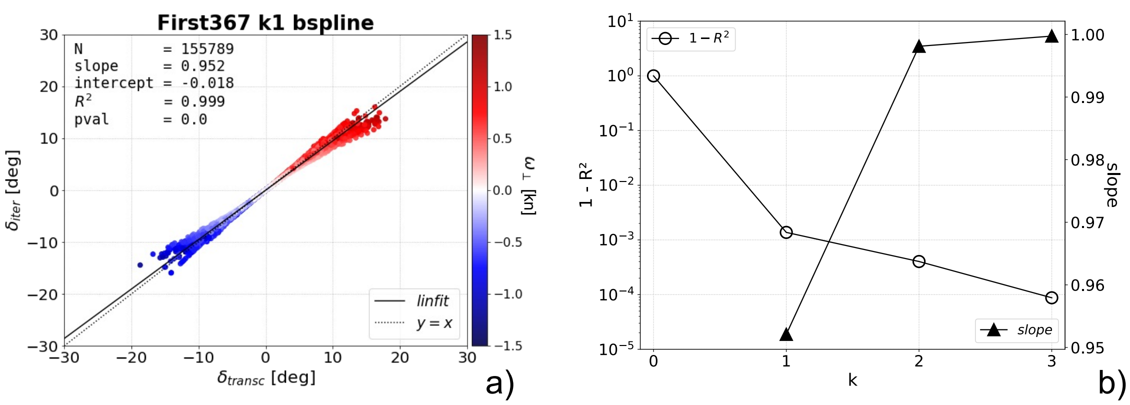

Figure A1. Approximate vs. exact solution of Eq. 13 for a First-367 sailboat. a) Iterative solution of Eq. A1 with $k = 1$ vs. the exact solution, using $\omega_\perp$ as marker colour; b) unexplained variance (R is the Pearson's correlation coefficient) of the linear regression and fitted slope coefficient for various k values.

https://doi.org/10.5194/egusphere-2023-2060
Preprint. Discussion started: 16 November 2023

Appendix B: Neural network features

For identifying the vessel performance curves from a LUT via a neural network, a multi-layer perceptron was used.

The models were built and trained via the `scikit-learn` package[§§§]. A three-fold cross-validation was used to identify the best model for each vessel performance function. Different solvers, hidden layers' sizes, L2 regularisation terms, and activation functions were explored, covering a search space of about 10^3 models. The optimal configuration made use of the rectified linear unit activation function, the Adam optimiser to minimise mean-squared error, for at most 10^3 passes through the training set ("epochs") with a batch size of 200, a constant learning rate of 10^{-4} and early stopping after the validation loss has failed to decrease for 10 epochs.

Author contributions. G.M.: Conceptualization, Funding Acquisition, Methodology, Project administration, Supervision, Validation, Writing – original draft, Writing – review & editing; M.L.S.: Data Curation, Investigation, Software, Validation, Visualization; L.C.: Data Curation, Investigation, Software, Validation, Visualization; N.P.: Investigation, Resources; J.O.: Investigation, Resources

Competing interests. The authors do not declare any competing interests.

Disclaimer. The authors are not liable for casualties nor losses occurred in using routes computed via VISIR-2 for navigation purposes.

Acknowledgements. Funding through both the Italy-Croatia Interreg projects GUTTA (grant number 10043587) and FRAMESPORT (10253074) is acknowledged. chatGPT-3 was used to review the English text in parts of this manuscript.

[§§§] https://scikit-learn.org/stable/

https://doi.org/10.5194/egusphere-2023-2060
Preprint. Discussion started: 16 November 2023

References

Al-Aboosi, F. Y., El-Halwagi, M. M., Moore, M., and Nielsen, R. B.: Renewable ammonia as an alternative fuel for the shipping industry, Current Opinion in Chemical Engineering, 31, 100 670, https://doi.org/https://doi.org/10.1016/j.coche.2021.100670, 2021.

Bentley, J. L.: Multidimensional binary search trees used for associative searching, Communications of the ACM, 18, 509–517, 1975.

Bertsekas, D.: Network Optimization: Continuous and Discrete Models, Athena Scientific, Belmont, Mass. 02178-9998, USA, 1998.

Bouman, E. A., Lindstad, E., Rialland, A. I., and Strømman, A. H.: State-of-the-art technologies, measures, and potential for reducing GHG emissions from shipping – A review, Transportation Research Part D: Transport and Environment, 52, 408–421, https://doi.org/https://doi.org/10.1016/j.trd.2017.03.022, 2017.

Breivik, Ø. and Allen, A. A.: An operational search and rescue model for the Norwegian Sea and the North Sea, Journal of Marine Systems, 69, 99–113, 2008.

Bullock, S., Mason, J., Broderick, J., and Larkin, A.: Shipping and the Paris climate agreement: a focus on committed emissions, BMC Energy, 2, 5, https://doi.org/10.1186/s42500-020-00015-2, 2020.

Carchen, A., Gaggero, T., Besio, G., Mazzino, A., and Villa, D.: A method for the probabilistic assessment of the on-board comfort on a passenger vessel route, Ocean Engineering, 225, 108 702, 2021.

Claughton, A.: Developments in the IMS VPP Formulations, in: Fourteenth Chesapeake sailing yacht symposium, Annapolis, Maryland, pp. 1–20, 1999.

Claughton, A. R.: Developments in hydrodynamic force models for velocity prediction programs, in: Proceedings of the International Conference The Modern Yacht, ISBN: 0 903055 91 0, Published by The Royal Institution of Naval Architects, RINA. Paper: P2003-4 Proceedings., 2003.

Dijkstra, E. W.: A note on two problems in connexion with graphs, Numerische mathematik, 1.1, 269–271, https://doi.org/10.1145/3544585.3544600, 1959.

DoS: Green Shipping Corridors Framework, Tech. rep., US Department of State, https://www.state.gov/green-shipping-corridors-framework/, 2022.

Faber, J., van Seters, D., and Scholten, P.: Shipping GHG emissions 2030: Analysis of the maximum technical abatement potential, Tech. rep., CE Delft, 2023.

Farkas, A., Parunov, J., and Katalinić, M.: Wave statistics for the middle Adriatic Sea, Pomorski zbornik, 52, 33–47, https://doi.org/10.18048/2016.52.02, 2016.

Filipiak, D., Węcel, K., Stróżyna, M., Michalak, M., and Abramowicz, W.: Extracting Maritime Traffic Networks from AIS Data Using Evolutionary Algorithm, Business & Information Systems Engineering, 62, 435–450, https://doi.org/10.1007/s12599-020-00661-0, 2020.

gov.uk: Clydebank Declaration, Tech. rep., UK Department for Transport, https://www.gov.uk/government/publications/cop-26-clydebank-declaration-for-green-shipping-corridors, 2021.

Guedes Soares, C.: Effect of heavy weather maneuvering on the wave-induced vertical bending moments in ship structures, Journal of Ship Research, 34, 60–68, 1990.

IMO: MEPC.304(72) Initial IMO strategy on reduction of GHG emissions from ships, Tech. Rep. Annex 11, International Maritime Organization, London, UK, 2018.

IMO: MEPC.80/(WP.12) Report of the Working Group on Reduction of GHG Emissions from Ships Report of the Working Group on Reduction of GHG Emissions from Ships, Tech. rep., International Maritime Organization, London, UK, 2023.

https://doi.org/10.5194/egusphere-2023-2060
Preprint. Discussion started: 16 November 2023

IPCC: Sixth Assessment Report, WG3, Ch.10, Tech. rep., IPCC, https://www.ipcc.ch/report/ar6/wg3/, 2022.

IPCC: AR6 Synthesis Report: Climate Change 2023, Tech. rep., IPCC, https://www.ipcc.ch/report/ar6/syr/, 2023.

Ladany, S. P. and Levi, O.: Search for optimal sailing policy, European Journal of Operational Research, 260, 222–231, https://doi.org/https://doi.org/10.1016/j.ejor.2016.12.013, 2017.

Le Goff, C., Boussidi, B., Mironov, A., Guichoux, Y., Zhen, Y., Tandeo, P., Gueguen, S., and Chapron, B.: Monitoring the greater Agulhas Current with AIS data information, Journal of Geophysical Research: Oceans, 126, e2021JC017 228, https://doi.org/10.1029/2021JC017228, 2021.

Li, H. and Yang, Z.: Incorporation of AIS data-based machine learning into unsupervised route planning for maritime autonomous surface ships, Transportation Research Part E: Logistics and Transportation Review, 176, 103 171, https://doi.org/https://doi.org/10.1016/j.tre.2023.103171, 2023.

Lolla, S. V. T.: Path planning and adaptive sampling in the coastal ocean, Ph.D. thesis, Massachusetts Institute of Technology, http://hdl.handle.net/1721.1/103438, 2016.

Maneewongvatana, S. and Mount, D. M.: It's okay to be skinny, if your friends are fat, in: Center for geometric computing 4th annual workshop on computational geometry, vol. 2, pp. 1–8, 1999.

Mannarini, G. and Carelli, L.: VISIR-1.b: ocean surface gravity waves and currents for energy-efficient navigation, Geoscientific Model Development, 12, 3449–3480, https://doi.org/https://doi.org/10.5194/gmd-12-3449-2019, 2019.

Mannarini, G., Lecci, R., and Coppini, G.: Introducing sailboats into ship routing system VISIR, in: 2015 6th International Conference on Information, Intelligence, Systems and Applications (IISA), pp. 1–6, IEEE, https://doi.org/10.1109/IISA.2015.7387962, 2015.

Mannarini, G., Pinardi, N., Coppini, G., Oddo, P., and Iafrati, A.: VISIR-I: small vessels – least-time nautical routes using wave forecasts, Geoscientific Model Development, 9, 1597–1625, https://doi.org/10.5194/gmd-9-1597-2016, 2016a.

Mannarini, G., Turrisi, G., D'Anca, A., Scalas, M., Pinardi, N., Coppini, G., Palermo, F., Carluccio, I., Scuro, M., Cretì, S., Lecci, R., Nassisi, P., and Tedesco, L.: VISIR: technological infrastructure of an operational service for safe and efficient navigation in the Mediterranean Sea, Natural Hazards and Earth System Sciences, 16, 1791–1806, https://doi.org/10.5194/nhess-16-1791-2016, 2016b.

Mannarini, G., Subramani, D., Lermusiaux, P., and Pinardi, N.: Graph-Search and Differential Equations for Time-Optimal Vessel Route Planning in Dynamic Ocean Waves, IEEE Transactions on Intelligent Transportation Systems, 21, 3581–3593,, https://doi.org/10.1109/TITS.2019.2935614, 2019.

Mannarini, G., Carelli, L., Orović, J., Martinkus, C. P., and Coppini, G.: Towards Least-CO_2 Ferry Routes in the Adriatic Sea, Journal of Marine Science and Engineering, 9, https://doi.org/10.3390/jmse9020115, 2021.

Mason, J., Larkin, A., and Gallego-Schmid, A.: Mitigating stochastic uncertainty from weather routing for ships with wind propulsion, Ocean Engineering, 281, 114 674, https://doi.org/https://doi.org/10.1016/j.oceaneng.2023.114674, 2023.

Orda, A. and Rom, R.: Shortest-path and Minimum-delay Algorithms in Networks with Time-dependent Edge-length, J. ACM, 37, 607–625, https://doi.org/10.1145/79147.214078, 1990.

Schroeder, K. and Chiggiato, J.: Oceanography of the Mediterranean Sea: An Introductory Guide, Elsevier, 2022.

Sidoti, D., Avvari, G. V., Mishra, M., Zhang, L., Nadella, B. K., Peak, J. E., Hansen, J. A., and Pattipati, K. R.: A Multiobjective Path-Planning Algorithm With Time Windows for Asset Routing in a Dynamic Weather-Impacted Environment, IEEE Transactions on Systems, Man, and Cybernetics: Systems, 47, 3256–3271, https://doi.org/10.1109/TSMC.2016.2573271, 2017.

Sidoti, D., Pattipati, K. R., and Bar-Shalom, Y.: Minimum Time Sailing Boat Path Algorithm, IEEE Journal of Oceanic Engineering, 2023.

Smith, T. and Shaw, A.: An overview of the discussions from IMO MEPC 80 and Frequently Asked Questions, Tech. rep., UMAS, 2023.

Svanberg, M., Ellis, J., Lundgren, J., and Landälv, I.: Renewable methanol as a fuel for the shipping industry, Renewable and Sustainable Energy Reviews, 94, 1217–1228, https://doi.org/https://doi.org/10.1016/j.rser.2018.06.058, 2018.

Tagliaferri, F., Philpott, A., Viola, I., and Flay, R.: On risk attitude and optimal yacht racing tactics, Ocean Engineering, 90, 149–154, https://doi.org/https://doi.org/10.1016/j.oceaneng.2014.07.020, innovation in High Performance Sailing Yachts - INNOVSAIL, 2014.

Theocharis, A., Balopoulos, E., Kioroglou, S., Kontoyiannis, H., and Iona, A.: A synthesis of the circulation and hydrography of the South Aegean Sea and the Straits of the Cretan Arc (March 1994–January 1995), Progress in Oceanography, 44, 469–509, https://doi.org/https://doi.org/10.1016/S0079-6611(99)00041-5, 1999.

van den Bremer, T. S. and Breivik, Ø.: Stokes drift, Philosophical Transactions of the Royal Society A: Mathematical, Physical and Engineering Sciences, 376, 20170 104, https://doi.org/10.1098/rsta.2017.0104, 2018.

Vettor, R. and Guedes Soares, C.: Development of a ship weather routing system, Ocean Engineering, 123, 1–14, https://doi.org/https://doi.org/10.1016/j.oceaneng.2016.06.035, 2016.

Wilson, G., Aruliah, D., Brown, C. T., Hong, N. P. C., Davis, M., Guy, R. T., Haddock, S. H., Huff, K. D., Mitchell, I. M., Plumbley, M. D., et al.: Best practices for scientific computing, PLoS Biol, 12, e1001 745, https://doi.org/10.1371/journal.pbio.1001745, 2014.

Zhou, P. and Wang, H.: Carbon capture and storage—Solidification and storage of carbon dioxide captured on ships, Ocean Engineering, 91, 172–180, https://doi.org/https://doi.org/10.1016/j.oceaneng.2014.09.006, 2014.

Zis, T. P., Psaraftis, H. N., and Ding, L.: Ship weather routing: A taxonomy and survey, Ocean Engineering, 213, 107 697, 2020.

https://doi.org/10.5194/egusphere-2023-2060
Preprint. Discussion started: 16 November 2023

Table 1. Graph resolution and number of edges. For graph order of connectivity ν, the angular resolution is given by $\Delta\theta = \arcsin(1/\nu)$. The number of non-collinear edges is denoted as N_{q1}, and the total number of edges in the first quadrant is $\nu(\nu+1)$.

ν	$\Delta\theta$ [°]	N_{q1}	$\nu(\nu+1)$
1	45.0	2	2
2	26.6	4	6
3	18.4	8	12
4	14.0	12	20
5	11.3	20	30
6	9.5	24	42
7	8.1	36	56
8	7.1	44	72
9	6.3	56	90
10	5.7	64	110

Table 2. Principal parameters of the ferry.

Name	Symbol	Value	Units
Length overall	LOA	125	m
Draft middle	T	5.3	m
Deadweight	DWT	4,050	t
Main engine power	P_{main}	4,000	kW
Main engine rated speed	n_{eng}	750	rpm
Service speed	v_S	19	kn

Table 3. Principal parameters of the sailboat (First-367).

Name	Symbol	Value	Units
Length of hull	L_{hull}	10.68	m
Draft	T	2.2	m
Displacement	∇	5,773	m^3
Rudder wetted surface	-	1.42	m^2
Keel wetted surface	-	3.31	m^2
Main sail area	-	38	m^2
Jib sail area	-	3.97	m^2
Spinnaker area	-	95	m^2

https://doi.org/10.5194/egusphere-2023-2060
Preprint. Discussion started: 16 November 2023

Table 4. VISIR-2 modules with their original names, purpose, and references within this paper. Modules #1-5 represent the core package.

#	Module name	Meaning	Reference
1	Grafi	graph geometry	Sect. 2.2
2	Campi	environmental fields	Sect. 2.3
3	Pesi	edge weights	Sect. 2.3
4	Tracce	shortest path	Sect. 2.4
5	Visualizzazioni	rendering	Sect. 2.6
6	Docs	documentation	-
7	GUI	graphical user interface	-
8	Navi	vessel performance	Sect. 2.5
9	PostProc	assessments of products	-
10	Utilità	various utilities	-
11	Validazioni	validation	-

Table 5. VISIR-2 motorboat route duration vs. oracles: The reference time for the Techy oracle corresponds to the duration found via VISIR-1. For the LSE oracle, a graph with the same features as Mannarini et al. (2019) was used. The relative error is defined as the relative discrepancy between the VISIR-2 results and the oracle. Here, L_0 and T_0 represent the length and time scales, respectively.

benchmark	ν	$1/(\Delta x)$	$\Delta\tau$	L_0	T_0	ref_time	V2_time	rel_err
	-	$1/°$	min	nmi	hr	T_0	T_0	%
LSE	2	94	30	126.5	7.809	1.762	1.773	0.617
LSE	3	134	30	126.5	7.809	1.766	1.753	-0.774
Techy	5	25	5	140.1	6.640	1.056	1.0563	0.028

Table 6. Optimal route durations T^* and route duration relative mismatch dT^* of VISIR-2 sailboat routes compared to openCPN ones, corresponding to the situation of Fig. 8. $k = 2$ and $\Delta\tau = 15\text{min}$ were used.

				wind				current + wind			
				Westbound		Eastbound		Westbound		Eastbound	
version	ν	$1/\Delta x$	$\Delta\Theta$	T^*	dT^*	T^*	dT^*	T^*	dT^*	T^*	dT^*
		[1/deg]	[deg]	[hr]	[%]	[hr]	[%]	[hr]	[%]	[hr]	[%]
VISIR-2	4	12	14	34.6	0.2	57.7	4.0	32.3	0.2	32.3	0.2
	5	15	11	34.5	0.0	57.2	3.2	31.6	-1.9	31.6	-1.9
	6	18	9	33.4	-3.4	56.4	1.8	31.0	-3.7	31.0	-3.7
	7	21	8	32.9	-4.7	55.4	-0.1	30.8	-4.3	30.8	-4.3
	8	23	7	32.9	-4.7	56.2	1.3	30.9	-4.0	30.9	-4.0
openCPN				34.6		55.4		32.2		32.2	

https://doi.org/10.5194/egusphere-2023-2060
Preprint. Discussion started: 16 November 2023

submodule	a [us]	b [-]	c [s]
dist_D	0.030	1.120	-
dist_tot	0.001	1.333	-
time_D	1.814	1.003	-
time_tot	1.111	1.031	-
CO2t_D	0.952	1.037	-
CO2t_tot	0.594	1.064	-
time_D_V1b	26.000	1.010	0
time_tot_V1b	1.200	1.180	60

Table 7. Fit coefficients of the $T_c = a \cdot DOF^b + c$ regressions for various components of `Tracce`, motorboat version. "D" stands for the Dijkstra's algorithm only, while "tot" includes the post-processing for reconstructing the voyage. All data refers to VISIR-2 but the $*$_V1b ones, referring to VISIR-1.b.

	ITPTO - FRTLN χ [%]					FRTLN - ITPTO χ [%]				
	70	80	90	100	avg	70	80	90	100	avg
wa	3.1	2.3	1.5	1	2.0	0.9	0.6	0.4	0.3	0.7
wa-cu	3.7	2.8	1.9	1.3	2.5	1.2	0.9	0.6	0.5	0.9

Table 8. Average relative savings of the CO_2 -optimal vs. the least-distance route (in %), for various engine loads (χ), considering just waves (wa) or also currents (wa-cu), for ferry routes between Toulon (FRTLN) and Porto Torres (ITPTO) as in Fig. 10. The χ-averaged values are also provided in the "avg" columns.

χ [%]	a [-]	b [-]	d_1 [%]	d_2 [%]
70	630	0.026	1.6	21.2
80	649	0.020	1.5	20.6
90	661	0.030	1.3	11.2
100	672	0.027	1.3	9.6

Table 9. Fit coefficients of $y = a \cdot [\exp(-x/d_1) + b \cdot \exp(-x/d_2)]$ on the data of Fig. 11.b.

https://doi.org/10.5194/egusphere-2023-2060
Preprint. Discussion started: 16 November 2023

	GRMON - TRMRM			TRMRM - GRMON		
	$-dT^*$	$N_f^{(g)}$	$N_f^{(o)}$	$-dT^*$	$N_f^{(g)}$	$N_f^{(o)}$
wi	3.0	263	1	3.0	300	1
wi-le	3.0	274	4	3.1	315	4
wi-cu	3.2	262	1	3.6	303	2
wi-cu-le	3.4	273	1	3.2	320	6

Table 10. Average relative time savings of the sailboat routes (in %), considering just wind (wi), or also various combinations of currents (cu) and leeway (le), for the sailboat routes between Monemvasia (GRMON) and Marmaris (TRMRM) as in Fig. 12. The number of failed routes for the geodetic $N_f^{(g)}$ or the optimal routes $N_f^{(o)}$ is also provided.